



HAL
open science

Etching of iron and iron–chromium alloys using ICP-RIE chlorine plasma

Guillaume Le Dain, Ferial Laourine, Stéphane Guilet, Thierry Czerwiec,
Grégory Marcos, Cédric Noel, Gérard Henrion, Christophe Cardinaud, Aurélie
Girard, Ahmed Rhallabi

► **To cite this version:**

Guillaume Le Dain, Ferial Laourine, Stéphane Guilet, Thierry Czerwiec, Grégory Marcos, et al..
Etching of iron and iron–chromium alloys using ICP-RIE chlorine plasma. *Plasma Sources Science
and Technology*, 2021, 30 (9), pp.095022. 10.1088/1361-6595/ac1714 . hal-03378471

HAL Id: hal-03378471

<https://hal.science/hal-03378471>

Submitted on 28 Oct 2021

HAL is a multi-disciplinary open access archive for the deposit and dissemination of scientific research documents, whether they are published or not. The documents may come from teaching and research institutions in France or abroad, or from public or private research centers.

L'archive ouverte pluridisciplinaire **HAL**, est destinée au dépôt et à la diffusion de documents scientifiques de niveau recherche, publiés ou non, émanant des établissements d'enseignement et de recherche français ou étrangers, des laboratoires publics ou privés.

Etching of iron and iron-chromium alloys using ICP-RIE chlorine plasma

Guillaume Le Dain

Université de Nantes, CNRS, IMN, 2 rue de la Houssinière, F-44322 Nantes, France.

Feriel Laourine

Université de Lorraine, CNRS, IJL, F-54000 Nancy, France.

Université Paris Saclay, CNRS, C2N, 10 Boulevard Thomas Gobert, F-91120 Palaiseau, France.

Stéphane Guilet

Université Paris Saclay, CNRS, C2N, 10 Boulevard Thomas Gobert, F-91120 Palaiseau, France.

Thierry Czerwiec

Université de Lorraine, CNRS, IJL, F-54000 Nancy, France.

Grégory Marcos

Université de Lorraine, CNRS, IJL, F-54000 Nancy, France.

Cédric Noel

Université de Lorraine, CNRS, IJL, F-54000 Nancy, France.

Gérard Henrion

Université de Lorraine, CNRS, IJL, F-54000 Nancy, France.

Christophe Cardinaud

Université de Nantes, CNRS, IMN, 2 rue de la Houssinière, F-44322 Nantes, France.

Aurélie Girard

Université de Nantes, CNRS, IMN, 2 rue de la Houssinière, F-44322 Nantes, France.

Ahmed Rhallabi

Université de Nantes, CNRS, IMN, 2 rue de la Houssinière, F-44322 Nantes, France.

E-mail: ahmed.rhallabi@cnrs-immn.fr

Abstract. Dry etching process of iron, chromium and iron-chromium alloys under a chlorine-based plasma is studied. The objective is to create new surface functionalities. The approach combines an experimental study of an ICP (Inductively Coupled Plasma) reactor with the development of a multi-scale etching model including kinetic, sheath and surface models. Results from plasma etching of substrates in *Fe*, *Cr* and made of *Fe – Cr* alloys are presented. Optical emission spectroscopy and interferometry measurements show strong modifications of the plasma when *Fe* or *Cr* samples are present in the reactor. It is shown that iron is easier to etch than chromium. The study highlights the role of chemical etching by the formation of volatile products such as *FeCl₃*. The chromium content in *Fe – Cr* alloys has a strong impact on both the lateral and vertical etch rates, as well as on the roughness along the profile. For *Fe – Cr* alloys, the experimental and calculated values of etch rate are very similar. The concept of hard zones is introduced to get a better agreement between simulation results and experimental ones. This good agreement demonstrates the capability of the developed simulator to implement new phenomena.

1. INTRODUCTION

The history of plasma etching began in the late 1960s when S. Irving set out to remove polymers using an oxygen plasma [1, 2]. Later, silicon etching by fluorine-based plasmas has been developed [3, 4, 5]. In 1979, Coburn and Winters highlighted the ions to neutrals synergy mechanism, opening the way to Reactive Ion Etching (*RIE*) processes to optimize the etch rates and control of the etch profile [6]. From this period, etching processes were constantly optimized and are more and more complex in order to meet the needs of the micro technology sector. Nowadays, numerous materials can be plasma-etched [7]. However, developing a dry etching process on substrates made of transition metals presents some difficulties due to very low vapour pressure for simple metallic compounds for temperatures lower than a few hundred degrees. The poor substrate/mask selectivity is also an issue. However, the patterning of metallic materials is currently arousing great interest by its numerous applications in biology, mechanics, optics, microfluidics and microelectronics [8, 9, 10, 11]. Stainless steels play a crucial role in sustainable development because they are durable, hygienic and recyclable [12]. In order to create micrometric or submicron size patterns on stainless steel surfaces, it is important to better understand the etching of the different metals that compose the material. The present study focuses on *Fe*, *Cr* substrates and *Fe – Cr* alloys, iron and chromium being the main components of stainless steels [13, 14, 15]. The investigation of the interactions of these elements with the plasma is crucial to study and understand the main etching mechanisms (chemical and physical components). This work is developed according to two approaches: an experimental study using an ICP (Inductively Coupled Plasma) reactor and multiscale modelling. Both approaches feed jointly the study of the interaction mechanisms between the active species of the plasma phase and the etched surfaces.

The section 2 of this paper is a literature overview about metal etching, mainly *Fe* and *Cr*, using chlorine-based plasmas, mainly *Cl₂*. The structure of the model is presented in section 3 and the experimental setup in section 4. Section 5 presents and discusses results on the etching of *Fe* and *Cr*. A study on the influence of the *Cr* content on the etching of *Fe – Cr* substrate is presented as well. This last study has not been reported yet in literature.

2. LITERATURE OVERVIEW

One of the first study dedicated to metal etching was made by Laegreid *et al.* [16], who measured the sputtering yields of different metals. Their results present close sputtering yields for transition metals such like *Cr*, *Fe* or *Ni* and higher sputtering yields for noble metals as *Ag* or *Au*. The measured sputtering yields are higher for metals than for silicon or carbon. Behrisch and Eckstein's book [17] presents numerous results about the sputtering threshold energy of elements.

Recently, Altieri *et al.* published a paper that summarizes different plasma mixture

interactions with different metals, especially *Cu* but also *Co*, *Fe* or *TiN* materials [18].

Other research works dealt with the etching of steel and metal alloys [19, 20]. Most of them were dedicated to plasma-wall interactions. Cunge *et al.* studied the deposition of etching byproducts $SiCl_x$ onto the reactor walls [21]. Until now, the studies shown that chlorine-based plasmas are good candidates for metal etching. Organic plasma mixtures can etch some metals, by pure ion bombardment process or in some cases by forming volatile organometallic compounds like CH_4 or C_3H_6O for example [22, 23, 24].

Plasma-surface interactions can be studied through a thermodynamic analysis focused on the chlorine/material chemical reactions [25]. It allows getting data about volatility of created products and the most likely reactions occurring onto the etched surface. The simulations can run with different gas mixtures. For example, if a fluorine based plasma does not form volatile compounds on *Cr*, these simulations can predict if adding H_2 or O_2 or another gas to this fluorine-based plasma can form CrF_xH_y or CrF_xO_y compounds, and check if these new species are volatiles. Altieri proved that *Fe* can form volatile compounds when it is exposed to *Cl* atoms in gaseous form [26].

For Cl_2 ICP plasma discharge, numerous studies exist, using trace rare gas optical emission spectroscopy to determine the electron temperature T_e [27, 28]. From these studies, T_e is relatively stable, between 2 and 4 eV for a large range of power (10-1000 W) and pressure (5-20 mTorr). Fuller *et al.* pointed out an increase in T_e with the argon percentage in Cl_2/Ar mixture [29], as well as a slow decrease of Cl^+ density [30]. Malyshev *et al.* published numerous papers, about the dissociation of Cl_2 [31] and the impact of the substrate bias on the plasma [32].

In addition, Efremov *et al.* made comparison between a global kinetic model and experiments for Cl_2/Ar plasma mixture [33, 34], showing a decrease in electron density, from $10^{11} cm^{-3}$ to $2 \times 10^{10} cm^{-3}$, when the argon percentage varies from 0 to 100 %.

Chanson *et al.* developed a global model of $Cl_2/N_2/Ar$ coupled to a Monte-Carlo cellular surface model for *InP* etching [35]. They showed the effect of the nitrogen percentage on the elimination of the bowing of the sidewall.

For iron etching, Cho *et al.* [36] demonstrated a rather high etch rate by using *IBr* and *ICl* plasmas. They measured an etch rate of 100-150 nm/min for *Ni* and *Fe* in some conditions. Andriessse *et al.* [37] observed a strong increase of *Fe* etch rate when the substrate temperature increases from 70 to 200 °C, while the etch rate slowly increases with bias from 0 to -75 V. XPS (X-Ray Photoelectron Spectroscopy) analyses revealed the presence of *Fe-Cl* bonds, proving the chemical adsorption of *Cl* on the surface etched by Cl_2/BCl_3 . Park *et al.* [38] evaluated the effect of Cl_2 percentage on the etch rate of *Fe* under Cl_2/Ar plasma. They observed a maximum of etch rate at 50% Cl_2 , and a strong increase of etch rate between 0 and 25% Cl_2 . These results, associated to Andriessse's ones [37] show that iron can be sensitive to chemical etching by neutral *Cl*, with a dependence on substrate temperature. $FeCl_3$ has a vaporization temperature of 316 °C at atmospheric pressure [39].

For chromium, Ebbinghaus *et al.* [40] showed the evolution of chloride, fluoride or oxychloride compounds of *Cr*, in terms of formation and volatility. Recently, Wu *et*

al. published a review about photomask plasma etching, with a part dedicated to *Cr* etching [41]. The first study dedicated to chromium etching was provided by Abe *et al.* [42]. They analysed the etching process using plasma mixtures with Cl_2 and O_2 and attributed it to the formation of $CrCl_2O_2$ volatile compounds ($CrCl_2O_2$ is volatile at room temperature [43]). Curtis *et al.* [44] studied the evolution of *Cr* etching by varying the percentage of O_2 in CCl_4/O_2 mixtures and observed a maximum of chromium etch rate for 50 % O_2 . Staaks *et al.* [45, 46] performed etching of *Cr* by using Cl_2/O_2 plasma, observing a maximum of etch rate for 20-40 % O_2 . By studying the substrate temperature impact, they showed a strong increase in etch rate, from 5 to 40 *nm/min* when the substrate temperature increased from -80 °C to 40 °C. This evolution can be due to chemical etching of *Cr*. The same behaviour was observed by Nakata *et al.* [47] and Ichiki *et al.* [48]. They also observed an undercut etching for *Cr* and an etch rate ten times higher for Cl_2/O_2 plasma mixture with a few % O_2 than for a pure Cl_2 plasma. Aydinoglu *et al.* [43] observed a higher etch rate for Cr_2O_3 substrate than for *Cr* substrate in the same conditions. This was attributed to the presence of native oxide for Cr_2O_3 . The presence of a $CrCl_xO_y$ layer after plasma etching was confirmed by XPS analyses [49].

3. MODEL

The model developed in this study is based on a multiscale approach including three different modules to track the etched surface evolution as a function of operating conditions: pressure, gas mixture, flow rates, power, bias, etching duration. This approach was already performed for the simulation of *InP* etching by $Cl_2/N_2/Ar$ plasma mixtures [35]. Multiscale approach has been developed by several authors [50, 51, 52, 53, 54].

Figure 1 shows our simulator flowchart in which the primary input data represent the machine parameters such as RF power, pressure, gas flow rates, DC bias and reactor geometry:

- Plasma module: it allows calculating the densities and fluxes of neutral and charged species as well as the electron density n_e and temperature T_e .
- Sheath module: it allows calculating the positive Ion Energy Distribution Function *IEDF* for different incident angles. Output data from plasma module in terms of n_e , T_e and positive ion flux fractions are introduced as input data in the sheath model. Indeed, n_e and T_e are required to evaluate the average sheath thickness using Langmuir theory while positive ion flux fractions are used to randomly select each ion type entering the sheath.
- Surface module: it allows calculating the steel etch profile evolution through a mask as a function of time. Output data from plasma and sheath modules in terms of Cl and positive ion fluxes and *IEDFs* are introduced in the surface module as input data.

3.1. Kinetic Model

Plasma kinetic model is applied to a Cl_2/Ar ICP. It is based on a 0D global approach [55, 56] to calculate the neutral and ion average densities and fluxes. It provides these values for the reactive species participating in the steel etching process. Details of the model formalism are given in [57, 58]. The reaction scheme was updated using data provided by several authors [59, 60]. Indeed, a recent publication of Hamilton *et al.* [61] presents new cross sections for the main reactions involved in Cl_2 molecule dissociation by electron impact. The mass balance equations, associated to each species (neutral and ion) considered in the reaction scheme, include the following mechanisms: reactions by electron impact, neutral/neutral, neutral/ion and ion/ion volume reactions, radiative deexcitation by photon emission and surface reactions.

$$\begin{aligned} \frac{\partial(n_j)}{\partial t} = & x_j \frac{N_o}{\tau} - n_e n_j \sum_l k_l(T_e) + n_e \sum_{l,m} k_l(T_e) n_m \\ & - n_j \sum_l k_l(T_{gas}) n_m + \sum_{l,m,i} k_l(T_{gas}) n_i n_m - k_s^j(p, T) n_j \\ & + \sum_r k_s^r(p, T) n_r - \frac{n_j}{\tau} \end{aligned} \quad (1)$$

The first term represents the injected gases where x_j , N_o and τ are the fraction of injected gas j , total gas density and residence time respectively. In the present case, $x_j \neq 0$ only for $j = Cl_2$ and Ar ($x_{Cl_2} + x_{Ar} = 1$). The second and the third terms are the loss and production rates of species j by electron impact. The fourth and the fifth terms are the loss and the production rates by volume reactions. The sixth and the seventh terms are the loss and the production rates on the wall surface and the last term in equation 1 is the loss rate by pumping. $k_l(T_e)$ is the reaction coefficient of reaction l by electron impact, $k_l(T_{gas})$ is the reaction coefficient of collision between i and m species. k_s^j is the reaction coefficient of species j on the surface. All these reaction coefficients are listed in annex, section 7.

The reaction coefficients by electron impact are calculated assuming a Maxwellian electron energy distribution function (*EEDF*). The calculation of such coefficients needs the knowledge of their associated cross sections. Details are given in [62, 63, 64, 65, 66] :

$$k_e(T_e) = \langle \sigma_e(\varepsilon) v_e \rangle = \int \sigma_e(\varepsilon) \sqrt{\frac{2\varepsilon}{m_e}} f(\varepsilon, T_e) d\varepsilon \quad (2)$$

where T_e is the electron temperature, v_e is the electron velocity, m_e is the electron mass, $f(\varepsilon)$ is the *EEDF* and ε is the kinetic energy of electrons.

For volume reactions, the rate coefficient can be written most of the time as follows :

$$k_v(T_{gas}) = c_1 \left(\frac{T_{gas}}{300}\right)^{c_2} \exp\left(\frac{-c_3}{T_{gas}}\right) \quad (3)$$

where c_1 , c_2 , c_3 are constant and T_{gas} is the gas temperature in K . c_1 , c_2 and c_3 can be evaluated using thermo-kinetic data [67]. In our case, c_3 is usually equal to zero, $1 < c_2 < 3$ and c_1 is around $10^{-9} \text{ cm}^3/\text{s}$ while it is around $10^{-36} \text{ cm}^3/\text{s}$ for three body

reactions. Gas temperature is calculated as a function of the gas pressure Pr and RF power P_{RF} [68]:

$$T_{gas} = 300 + 1250((1 - e^{(-91Pr)}) + 400 \times e^{(-337Pr)}) \frac{1}{3.69} \ln\left(\frac{\alpha P_{RF}(V_D)}{40V}\right) \quad (4)$$

where α is the fraction of absorbed power (estimated to be 0.75), V_D the volume of Donnelly's reactor and V the volume of reactor considered in simulations [69].

For deexcitation reactions, we refer to Singh *et al.* works for the estimation of the average loss rate [70]. For surface reactions, we use a formalism developed by Chantry [71]. Note that surface reactions, especially those involving atoms, have been studied for different plasmas [72, 73]. The present plasma kinetic model does not take into account the desorbed particles from the etched surface. It is assumed that their concentrations are lower than those of the species produced from the injected gases. The complete reaction scheme is presented in section 7

A 0D model cannot study spatial variations that occur in the plasma sheath. Hence, the calculated output data, in terms of ion fluxes and electron temperature and density, are introduced as input data in the sheath model.

3.2. Sheath Model

We use a sheath module to study the positive ion transport through the sheath. Located between the plasma and the substrate, the sheath zone is characterized by an electron depletion due the high electron mobility in comparison to that of the positive ions. This induces a change in the electric field leading to the acceleration of positive ions across the sheath. When the DC bias increases, the electrical field in the sheath becomes stronger.

To determine the evolution of the electric field in the sheath, a simple analytic formula has been proposed by Manenschijn *et al.* [74] assuming that the electric field is perpendicular to the substrate surface:

$$E(z, t) = V_{CS}(t) \frac{n}{l_s} \left(\frac{z}{l_s}\right)^{n-1} \quad (5)$$

where z is the axial coordinate ($z = 0$ at the sheath entrance), n is constant between 0.5 and 1. In our simulations, n is estimated to 0.75. l_s is the sheath thickness that depends on T_e and n_e ; it is evaluated from the plasma model [75]. The potential drop across the sheath (V_{CS}) depends on the DC bias [75].

To calculate the ion energy at the entrance of the sheath, we used a formula proposed by Kokkoris *et al.* [76].

The simulation is based on Monte-Carlo 3D algorithm. The considered positive ions are randomly selected regarding their fractions compared to the total positive ion flux. As an example, for a given ion, such as Cl^+ , with 33 % of the total ion flux, the probability to select it is 0.33. Then, initial position and angle of each selected ion are randomly chosen at the entrance of the sheath. Its trajectory is then calculated using

Newton's law and knowing the electric field evolution versus the axial position and time [74]. When the ion reaches the substrate surface, its angle and energy are stored.

By following the trajectories of many ions (a high number of Cl_2^+ , Cl^+ and Ar^+ for a Cl_2/Ar discharge), 10^5 to 10^6 ions, the Ion Energy Distribution Functions (*IEDFs*) can be determined for different incident angles (from 0° , normal to the surface, to 90° , parallel to the surface). The calculated *IEDFs* are introduced in the surface model as input data.

3.3. Surface Model

The main part of this study uses a Monte-Carlo 2D cellular algorithm. Details can be found in several papers [77, 78, 79]. The model simulates interactions between superparticles, that represent reactive neutrals and ions from plasma, and supersites, that represent surface atoms. The simulation area, composed of substrate and mask, is represented in 2D cartesian coordinate system (x, y) (see figures 2-3). This pattern is taken as representative of all the features over the surface of a real sample.

The surface properties are set by the user: vertical and lateral dimensions of the whole considered system, mask thickness and aperture, mask sidewalls. This 2D simulated area is completely divided into square supersites, with dimensions provided by the user, which represents a finite amount N of real atoms. N is determined using dimensions of supersites, chemical composition of the substrate and atomic densities:

$$N = N_A(\delta * 10^{-4})^3(\%Fe \frac{\rho_{Fe}}{M_{Fe}} + \%Cr \frac{\rho_{Cr}}{M_{Cr}}) \quad (6)$$

where N_A is Avogadro's number, δ is the lateral dimension of a supersite in μm , typically $3.231 \times 10^{-3} \mu m$, ρ the volumic mass and M the molar mass.

For this study, iron and chromium are the two main elements considered for the substrate, whereas the mask is made of silica. Three types of solid supersites are therefore on the simulation area when a new simulation begins: Fe , Cr and SiO_2 . The positions of Fe and Cr in the initial matrix are randomly generated regarding their fractions. The areas without atoms are represented by empty supersites with the same dimension as the others.

The mechanisms describing interactions between plasma superparticles and surface supersites are based on survey methods. The principle is as follows: an interaction between a plasma superparticle (atom or ion) with a supersite is considered representative of the interactions between N species from the plasma and N surface sites of the same nature.

Figure 3 is an overview of different superparticle-surface site interactions considered in the model: adsorption/desorption, sputtering and redeposition. All of these processes are introduced in a probabilistic way. Table 1 gives the probabilities for chlorine atoms adsorption on iron or chromium sites to form $FeCl_x(x = 1 - 3)$ or $CrCl_x(x = 1 - 2)$ compounds. Probabilities for redeposition of etched sites are thus listed. Srivastava *et al.* underlined the possible role of unpaired electrons on the sticking coefficient of

$SiCl_x(x = 1 - 4)$ compounds, which is lower for $SiCl_2$ or $SiCl_4$ onto reactor walls than for $SiCl$ or $SiCl_3$ [80]. Deposition probabilities of $FeCl$ and $CrCl$ sites could thus be different of the deposition probabilities of $FeCl_2$ and $CrCl_2$. On iron sites, the successive chlorine atom adsorptions lead to the formation of the $FeCl_3$ compound that is volatile and thus spontaneously desorbs (see figure 4) while the spontaneous desorption is not allowed for $CrCl_x(x = 0, 2)$. Indeed, the successive adsorptions of Cl onto chromium sites form only non volatile $CrCl_2$. If the adsorption process of the neutral reactive particle (Cl in our case) on the neighboring site does not occur, the particle reflects, with a randomly generated direction, into another etched surface. Redeposition concerns only sputtered surface supersites. After sputtering, a direction is randomly selected using a sinusoidal probability distribution centered on the direction of impinging/sputtering ion. Finally, after interactions, there is a displacement procedure in the model. It is a security procedure that moves the supersites on the sidewalls if empty sites are present. This is because some supersites are only sensitive to ion bombardment, so, in the area under the mask, they cannot be etched. This can lead to the formation of supersites surrounded by voids, which is not relevant. So, displacement takes care of it and moves the supersites in prevention.

During ion bombardment, a large part of incident energy is transmitted to the surface and produces sputtering mechanisms. This atom ejection creates defects onto the surface, especially dangling bonds, and a part of ion energy is transmitted to the non-ejected surface atoms. Due to these dangling bonds and energy, some surface atoms can desorb according to thermodynamics. Moreover, the surface defects make easier the adsorption of reactive neutrals onto the surface. This enhancement of adsorption is calculated by the introduction of a probability, named P_{des} , initially equal to 0. P_{des} is increased by 0.04 for the first neighbours that surrounded a sputtered site. This is taken into account in the model, as shown the red rectangle in figure 3. Both $FeCl_x(x = 0 - 2)$ and $CrCl_x(x = 0 - 2)$ are sputtered or desorbed by ion bombardment.

Sputtering yields introduced in the model are listed in table 2. They are calculated from SRIM software [81] by varying incident ion energy and angle (see figure 5). The same sputtering yield is taken for Fe and $FeCl_x(x = 0 - 2)$, ditto for Cr and $CrCl_x(x = 0 - 2)$. The right column of table 2 presents the sputtering data of hard zones. It is a specific concept used to describe the etching mechanisms for $Fe - Cr$ alloys and described in section 5. In the model, a hard zone represents the first Fe supersites neighbours of Cr supersites or the first Cr supersites neighbours of Fe supersites. Figure 6 shows the numerical treatment in the model that represents this phenomenon of hard zones. These hard zones are a procedure implemented in the model to simulate a strong reduction of etch rate in some conditions. This reduction is assumed to be linked to a low ion/surface energy transmission, due to interactions between Fe and Cr elements. The effects are similar to those of etch inhibitors, studied and simulated by Kokkoris *et al.* [82, 83]. But the origin of these etch inhibitors is the deposition of species from the reactor walls, mask or electrode for hard inhibitors and the deposition of species from plasma for soft inhibitors. Hard zones described in this study are thus different of these

inhibitors. Hard zones are also different of micromasking effect, which is rather due to the local redeposition of etched compounds. Such compounds are resistive to chemical etching. [84, 85]

4. EXPERIMENTAL SET-UP

Experiments were performed in an ICP/RIE SENTECH SI500 plasma reactor represented in figure 7, according to the different conditions given in table 3. The samples are placed on an Al_2O_3 substrate holder.

Studies on *Fe* and *Cr* pure elements were realized on 250 μm thick iron sheets (99,5 % pure) from Goodfellow and on a 3 mm thick massive chromium substrates produced in an evaporation machine. For the *Fe* – *Cr* alloys, studies were performed on 3 mm thick samples with 0, 1, 3, 5, 8, and 12 wt (weight) % of *Cr*. Before etching, *Fe* and *Cr* samples were mirror polished with *SiC* paper until 2400 granulometry, then with a diamond suspensions containing grains of 3 μm then 1 μm . Samples were masked by PECVD with a 1 μm thick *SiN* mask. *Fe* – *Cr* alloys were also mirror polished and masked by PECVD with a 500 nm thick *SiO₂* thin layer. All samples were patterned by optical lithography. After the etching step, the remaining *SiO₂* and *SiN* masks were removed by *SF₆/CHF₃* plasma, in the same reactor. Then, etch rates were calculated by dividing the average depths measured on every etched sample by the etching time.

The average etched depth was calculated over 3 steps height, measured on patterns after etching and removal of the remaining *SiN/SiO₂* mask. These measurements were carried out using a contact profilometer DEKTAK8 with a stylus of 5 μm .

Between each etching run, the ICP/RIE reactor was cleaned by a standard cleaning recipe consisting in 3 steps as shown in table 4. Optical emission spectroscopy (OES) measurements were performed during iron and chromium etching through the reactor quartz windows. A TRIAX500 (Jobin-Yvon) equipped with a CCD detector and a diffraction grating with 1800 lines/mm was used for this study. The aperture of the entrance slit was 50 μm , the exposure time was 50 ms. Spectra were recorded over the wavelength range from 300 to 900 nm. The identification of the emission lines was done using available databases [86], [87].

Plasma electron density (n_e) was measured by a microwave interferometer Miwitron MWI2650. Interferometry is a non-perturbative technique that allows determining the electron density from the phase shift of the microwave propagating through the plasma with respect to the incident wave. The interferometer used works at a frequency of 26.5 GHz, which fixes an upper limit at about $9.10^{12} cm^{-3}$ for n_e to be measured. The accuracy is of 0.1°, which corresponds to $10^9 cm^{-3}$ in electron density for a plasma length of 55 mm [88].

5. RESULTS AND DISCUSSION

This part presents the results about *Cl₂* plasma etching of *Fe*, *Cr* and *Fe* – *Cr*

alloys. Section 5.1 is dedicated to the analysis of Cl_2 plasma properties evolution with pressure and power. This study presents results from simulation and experiment results without introducing metallic samples in the chamber. Section 5.2 presents the effect of the metallic substrate on the plasma properties using microwave interferometry and optical emission spectroscopy. Section 5.3 presents experimental etch rates of Fe and Cr as well plasma surface interactions deduced from experiments. Section 5.4 exposes the simulation results showing the effect of Cl adsorption probability on the Fe etching evolution. Section 5.5 shows comparison between experimental and simulated etch rates of $Fe-Cr$ alloys. Finally, section 5.6 draws the effect of Cr content on the morphological properties of etched patterns as well as the etched product evolution.

5.1. Plasma properties: Simulation results vs experimental results

Figure 8 shows the electron density evolution with RF power for 5 and 20 *mTorr* pressure. Electron density increases when the RF power increases because of higher ionization processes. However, for RF power lower than 500 *W*, a decrease in n_e with the pressure is observed. In this power range, a significant part of collisions is responsible of the negative ion production to the detriment of the production of free electrons. Such production is due to dissociative attachment of Cl_2 by electron impact (reaction R_{14}). This can be explained by the fact that, for RF power lower than 500 *W*, Cl_2 dissociation rate is rather low and then Cl_2 is still the dominant species favoring the attachment process (figure 9). Over 500 *W* RF power, Cl_2 dissociation rate gets higher and higher as the power increases and Cl atom becomes the dominant species in the plasma. This favors the ionization of Cl while the attachment process on Cl_2 through the reaction R_{14} (see section 7) gets less important. A satisfactory agreement between the simulation and the measurements is obtained for 5 *mTorr* pressure. An experimental estimation of the Cl_2 dissociation rate can be obtained by optical actinometry using xenon as an actinometer [89]. The Xe I line at 823.1 *nm* (transition $5p^5(^2P_{3/2}^o)6s \rightarrow 5p^5(^2P_{3/2}^o)6p$) was used; the energy of the upper level of the transition lies at 9.83 eV. Regarding chlorine atoms, the Cl I line at 837.6 *nm* (transition $3s^23p^4(^3P)4p \rightarrow 3s^23p^4(^3P)4s$) was chosen since its upper level energy (10.4 eV) is close to that of the Xe transition. Malyshev and Donnelly also reported that all Cl lines in the range 700-900 *nm* follow the same variation with increasing *RF* power [89].

Malyshev and Donnelly [89] also showed that under similar conditions than those used here, the plasma is strongly dissociated and that the contribution of dissociative excitation by electron impact on Cl_2 on Cl line emission is very low. As the excitation cross sections of Cl lines by electron impact from the ground state are unknown, it is estimated that the line ration I_{Cl}/I_{Xe} is proportional to the density of Cl atoms as reported in [89]. The dissociation rate, defined as $[Cl]/[Cl_2]$ is then proportional to the I_{Cl}/I_{Xe} and is qualitatively compared to the calculated one in figure 9.

It is evidenced that the ion to neutral flux ratio plays an important role in the plasma etching. The nonlinear dependence of the etch rate on this ratio was already

pointed out because of the ion-neutral synergy in the etching process [90]. The physical etching under ion sputtering is more important as the ion to neutral flux ratio gets higher. Conversely, a low value of this ratio favors the pure chemical etching. Figure 10 presents the ion to neutral flux ratio versus the power for 5 and 20 *mTorr* pressure. For 5 *mTorr*, an almost linear variation of ion to neutral flux ratio with RF power is observed. However, for 20 *mTorr*, as n_e in figure 8 case, ion to neutral flux ratio is relatively lower at 20 *mTorr* than at 5 *mTorr* for RF power lower than 500 *W* while the trend changes beyond 500 *W*. This change is due to the increase of the ionization process of *Cl* to the detriment of the production of Cl^- by electron impact dissociative attachment of Cl_2 . Therefore, the ionization of *Cl* by producing Cl^+ is well favored because of the significant increase of the Cl_2 dissociation percentage (figure 9).

5.2. Impact of etched metals onto plasma properties

Figures 11-a and 11-c show optical emission spectra obtained of a reference chlorine plasmas (Cl_2 60 *sccm*, *Xe* 7 *sccm* at 4.8 *mTorr*, 800 *W* and -150 *V* of bias without substrate heating) with no metallic sample on the sapphire substrate holder. *Xe* was introduced in small quantity in the discharge as actinometer in order to estimate the atomic chlorine density. As expected in ICP chlorine plasma [91] most of the observed transitions belong to *Cl* I spectrum together with some line from Cl^+ , Cl_2 and Cl_2^+ . These reference spectra were recorded just before the etching experiments. When metallic sample are placed on the substrate holder, spectra reveal the presence of *Cr* I (figure 11-b) and *Fe* I (11-d) lines in the plasma. This confirms the capability of chlorine ICP plasma to etch iron and chromium.

Spectra show a strong decrease of the emission intensities for Cl_2 plasmas with iron samples. The line ratio I_{Cl}/I_{Xe} however does not change so much, it varies from 2.05 to 2.07 for the reference plasma and the plasma with the presence of *Cr* respectively and from 1.67 to 1.74 for the reference plasma and the plasma with the presence of *Fe* respectively. Electron density values determined by microwave interferometry are plotted in figure 12. The phase change error of interferometer is 0.1° , thus the error for n_e estimation is $8.4 \times 10^8 \text{ cm}^{-3}$. The accuracy of phase variation is 0.1° , which give an accuracy in n_e measurements of $8.4 \times 10^8 \text{ cm}^{-3}$. The error due to spatial variations of n_e into plasma chamber has not been estimated. Therefore, no error bars have been included in figure 12. The number 1 indicates the reference density, in chlorine plasma (conditions table 3), obtained just after reactor cleaning (see detailed procedure in table 4), without introducing a metallic sample or heating. Data points 2 to 5 were measured after the introduction of a chromium substrate (temperature at 150 and 220 $^\circ\text{C}$; points 2 and 3) then an iron substrate (points 4 and 5; same temperatures). Point 6 depicts a second reference point obtained just after iron removal and before the reactor cleaning. These data show a drop in the electron density induced by the presence of metallic sample. This drop is more significant for both iron and higher temperature. During etching, the formation and ejection of $FeCl_x (x = 0 - 3)$ or $CrCl_x (x = 0 - 2)$ from

metallic sample will contaminate both the chlorine plasma and the reactor walls. As shown previously, under the same conditions the etch rates of iron are greater than chromium. Consequently, contamination induced by iron containing etchant products is expected to be more significant, worsening when the temperature rises. These species strongly modify the electrical parameters of the plasma, including the electron density. The pollution of reactor walls is also the cause of these trends. During the experiments, they become covered with etching products that can subsequently desorb and enter again into the plasma phase. This is why n_e (figure 12, point 6, before reactor cleaning) does not rise to the initial value (point 1), but at a level close to that measured during the etching of iron at 220 °C.

To explain this drop of electron density, two mechanisms are assumed. Firstly, $FeCl_3$ species has a calculated electron affinity of 3.90 eV [92], a value that is even higher than those of Cl which is 3.61 eV from NIST database. It is possible that an electronic attachment process becomes more efficient leading to the production of negative ions to the detriment of electron population. Secondly, the polyatomic aspect of etchant products in the plasma phase would increase the power loss under excitation and dissociation by electronic impact of these etchant products. This would increase the effective creation energy of an electron-ion pair [93]. But due to a lack of etchant product data in terms of cross sections of reactions by electronic impact, it is difficult to confirm these hypothesis.

5.3. Experimental results: etching mechanisms of Fe and Cr

Pure *Fe* and *Cr* substrates were submitted respectively to argon and chlorine ICP plasmas, in conditions depicted in table 3. Etch rates are summarized in table 5. Under argon, the results are very close. In this case, the etching is due to pure sputtering mechanisms induced by Ar^+ ions. Calculations performed by SRIM show that sputtering yields of *Fe* and *Cr* are very similar. Under chlorine plasma, etch rate increases more for iron ($\times 6.7$) than for chromium ($\times 1.7$). According to results of the kinetic model and from OES, Cl^+ and Cl are respectively the major ionic and reactive neutral species, hence the ones participating to the etching mechanisms. Cl atoms can form $FeCl_x$ ($x = 1 - 3$) species or $CrCl_x$ ($x = 1 - 2$) species after surface adsorption of chlorine. According to the data in figure 4, this process is expected to form $FeCl_3$, a volatile product for the present operating pressure and surface temperature. The formation of gaseous compound by successive adsorption of Cl is known as chemical etching. Iron is thus exposed to both chemical and physical etching. On the other hand, chemical etching is not possible for chromium in the tested conditions, the process temperature being too low to form gaseous compounds (see figure 4). $FeCl_x$ ($x = 1 - 2$) and $CrCl_x$ ($x = 1 - 2$) compounds are sputtered by Cl_2^+ and Cl^+ ions, as well as iron and chromium. $FeCl_x$ ($x = 0 - 2$) and $CrCl_x$ ($x = 0 - 2$) species can spontaneously desorb from the surface only in the areas exposed to ion bombardment. In these zones, the formation of dangling bonds at the surface improves the adsorption of neutral chlorine

onto $FeCl_x(x = 0 - 2)$ and $CrCl_x(x = 0 - 2)$ surface sites. This process is taken into account in the surface model.

5.4. Etching of iron: Impact of Cl adsorption. Simulation results

The used RF bias (-150 V) is higher compared to some ICP etching processes [21, 94, 95, 96, 97]. Furthermore, the ion to neutral flux ratio $\Gamma_{ions}/\Gamma_{Cl}$ is relatively high (about 38%). In these conditions the physical etching is the dominant etching mechanism due to the efficiency of ion bombardment.

Both energy and number of ions by second are really high in this kind of machine. As a first approximation, the sputtering yields of $FeCl_x$ and $CrCl_x$ ($x = 1 - 2$) are supposed equal to those of original sites Fe and Cr . The adsorption of Cl on Fe sites accelerates the etching process. As explained in section 3, in the area exposed to ion bombardment, the adsorption probability of atomic chlorine increases and spontaneous desorption of surface sites occurs.

Figure 13 shows the effect of the adsorption probability ($P_{ads}(Cl)$: 0.1 to 0.4) at the $FeCl_x$ sites ($x = 0 - 2$) on the etch profile evolution. For a fixed etching time (2 min) of iron, the simulations show that the trench is deeper when $P_{ads}(Cl)$ is maximum. The increase of this surface parameter enhances the $FeCl_x(x = 0 - 2)$ formation. In the trench bottom, where the surface is submitted to the directional ion bombardment, a high chlorine adsorption improves reactive ion etching processes. Moreover, as neutral species have an isotropic distribution, increasing adsorption probability enhances $FeCl_x(x = 1 - 3)$ sites formation along the trench sidewalls. These zones are thus subjected to an important chemical etching process due to the formation of $FeCl_3$ species desorbing from the surface. The consequence is the formation of undercut and bowing defects, as shown in figure 13.

5.5. Etching of Fe-Cr alloys : Experiment and simulation

To analyse the effect of the chemical composition of $Fe - Cr$ alloys on the etching processes under Cl_2 plasma, we have performed simulation and experiment series by varying %wt of Cr from 0 to 12 (see table 3).

Figure 14 shows that the increase of the %wt of Cr leads to the decrease of the etch rate of $Fe - Cr$ alloy. The experimental etch rates are 244, 129, 67 nm/min for 0, 3 and 12 %Wt of Cr respectively. Both the simulations and the experiments show the same variation trend. However, the simulated etch rates are slightly higher than those obtained by experiment. The decrease in etch rate is particularly sharp between 0 and 5 %wt of chromium, then slows down to stabilize above 12% of Cr . This non-linear evolution indicates that the mechanisms involved are not limited to differences in etch rates between iron and chromium.

To explain this result, it is necessary to consider the existence of a global phenomenon resulting from the simultaneous presence of iron and chromium. We thus introduce the concept of hard zones to take into account of this interaction effect between

iron and chromium on the etching mechanisms. These hard zones therefore have better resistance to etching. Since it is unlikely that chemical etching decreases as much with such low chromium contents, we assume that surface mechanisms linked to ion bombardment are affected by a lower transmission of ion / substrate energy. Thus, in these hard zones the sputtering yields decrease and the assistance provided by the ion bombardment to the surface desorption of compounds is less efficient. Physical origin of these hard zones states that the inclusion of *Cr* into *Fe* would increase the hardness of the material and modify the surface energy. The subsequent modification of surface energy will lead to lower sputtering yield than for pure *Fe* or pure *Cr*. In the same time, the dislocation along the surface and the creation of defects are limited. This will impact the spontaneous desorption of *Fe* and *Cr* as well as the favorable adsorption of *Cl* atoms onto *Fe – Cr* surface. Once a sufficient chromium content is reached, the surface is covered by these hard areas and the etch rate settles down.

The surface model introduces this concept (see section 3 and table 2). Figure 14 clearly shows that the simulation results correlate well with the experiments, which supports our hypotheses. This accuracy has been obtained after the adjustment of numerical parameters into the model.

Figure 15 shows three simulated trenches obtained respectively for 0, 8 and 20 %wt of chromium (see table 3 for operating conditions). The third result is particularly interesting since it is similar to the case of austenitic steels which generally have a chromium content of around 16 %wt. For pure iron, even a global anisotropic aspect, the trench profile is characterized by the formation of lateral defects: bowing and undercut. Its depth is about 565 nm. The addition of chromium leads to the reduction (figure 15-b) or even to the elimination of these defects (figure 15-c).

At the trench bottom, the so introduced hard zones induce the formation of a significant roughness (figure 15-b) that is reduced when the percentage of chromium exceeds a certain threshold. From the results of figure 14, this threshold can be set at around of 12 %wt. As explained previously, the hard zones existence lowers the sputtering yields leading to the decrease of vertical etch rate.

5.6. Etching of Fe-Cr: Simulation results

In figure 16 the variations of simulated etched surface roughness and undercut level versus chromium percentage are plotted. Lateral dimension of a supersite is 3.231 nm. The roughness is calculated in the trench bottom by averaging the height of the peaks and valleys on either side of a baseline. This surface parameter varies from 15 to 40 nm, that is 5 to 12 supersites. There is a maximum roughness for 3 %wt chromium followed by a constant decrease until reaching a value lower than that measured for pure iron. A low chromium content induces the formation of hard zones that increase roughness by decreasing locally the sputtering and spontaneous desorption. When their distribution begin to recover the surface on the trench bottom, the interaction processes become more homogeneous as well and the roughness decreases.

The undercut is almost constant with *Cr* content less than 3 %wt (around 50 nm) and decreases for *Cr* content greater than 3 %wt up to 20 %wt (22 nm for 20 %wt of *Cr*). On the sidewalls, chemical etching is the dominant surface process because sputtering or assisted desorption are induced by ion bombardment that is almost directional. According to sheath model the angular shift is 2.5° around the normal to the sample surface. So, just under the mask, chromium sites cannot be etched. For sufficient content, the chromium sites homogeneously cover the trench sidewalls, creating a passivation layer reducing lateral etching processes. This has a positive effect on the profile anisotropy.

With this model, it is possible to count the different occurrences during one etching process. The variations of desorbed sites from iron or chromium surface are plotted in figures 17-a and 17-b. It shows the desorption of $FeCl_x(x = 0-3)$ and $CrCl_x(x = 0-2)$ due to chemical etching or ion bombardment. For the two figures, the d letter means spontaneous desorption (comprising chemical etching for $FeCl_3$), whereas sp means physical sputtering. A constant decrease of desorbed species is observed when the chromium content increases. For iron (see figure 17-a), etching is dominated by the formation of gaseous $FeCl_3$, while sputtering of $FeCl_x(x = 0-2)$ is consequent: iron sites are the most sputtered, because they are numerous in the alloys considered, followed by $FeCl$ and $FeCl_2$ sites. Desorption of non-volatile compounds $FeCl_x(x = 0-2)$ is very low. Furthermore, creation of gaseous $FeCl_3$ is favoured by the greater adsorption of Cl onto $FeCl_x(x = 0-2)$ in the areas exposed to ion bombardment. This synergy makes understandable the dominance of $FeCl_3$ formation and sputtering of $FeCl_x(x = 0-2)$ into the etching processes.

Spontaneous desorption of non gaseous $CrCl_x(x = 0-2)$ (see figure 17-b) is very low in comparison, nearly equal to zero. In the reaction scheme introduced in the model, successive adsorptions of chlorine atoms into the same supersite lead to the formation of stable $CrCl_2$.

For chromium (see figure 17-b), etching is largely dominated by sputtering mechanisms, with a great proportion of sputtered $CrCl_2$ sites. Due to the low chromium content into the substrate, chromium is expected to be always surrounded by some iron sites. Hence, for chromium into *Fe-Cr* alloys, adsorption is not favoured by ion bombardment but sputtering and spontaneous desorption are negatively affected by the phenomena of hard zones described in the previous section. Consequently, before its ejection from surface due to ion bombardment, chromium transforms to $CrCl$, then $CrCl_2$.

6. CONCLUSION

This work presents a joint experimental and modeling study of the dry etching of *Fe-Cr* alloys. An etching model of *Fe-Cr* alloy is developed. The model is composed of three modules: a plasma kinetic model, a sheath model and a surface model. With this multiscale approach, it is possible to predict the etch profile evolution of *Fe-Cr*

alloys through the mask versus the external ICP parameters.

The substrate temperature influences the volatility of compounds because of the difference in the boiling temperatures of pure elements and the chlorinated compounds. Knowledge of vapor pressure for these compounds helps establishing reaction scheme.. The differences in *Fe* and *Cr* etch rates while exposed to Cl_2 or *Ar* plasma is due to the formation of volatile $FeCl_3$ compounds and $CrCl_2$ non-volatile compounds onto the surface. This hypothesis has been reinforced by OES and interferometry measurements of Cl_2 plasma alone and during *Fe* and *Cr* etching. This corresponds to the data from literature and to the evolution of the vapour pressure of chlorinated compounds. *Fe* and *Cr* are both sensitive to physical etching by ion bombardment and chlorinated *Fe* and *Cr* species are created onto surface. The differences between surface energies of pure metals and chlorinated metals can increase the removal of these metals, hence the etch rate.

Based on model results, a preponderance is established of chemical etching for *Fe* by creation of gaseous $FeCl_3$ while sputtering of *Fe* and $FeCl_x$ ($x = 1 - 2$) is high. For *Cr*, sputtering of $CrCl_2$ is dominant. For iron, spontaneous desorption of non volatile surface compounds is low while, for chromium, it is almost negligible.

The diminution of etch rate by increasing *Cr* percentage, measured by profilometry and estimated by simulation, is also explained by the creation of hard zones around *Fe* sites due to the presence of *Cr* sites. These hard zones strongly decrease the etch rate because sputtering yield as well as spontaneous desorption probabilities decrease. Etching of steels using chlorinated plasma is an interesting way to functionalize steel surfaces with submicron pattern. As an immediate perspective, analyses of etched surface by XPS is need to validate our hypothesis and improve both our model and our understanding of chlorine plasma interactions with metal alloys.

Acknowledgement

This study is financially supported by French National Research Agency (ANR) through ANR-17-CE08-0029 project. This work was partly supported by the French RENATECH network.

- [1] S. M. Irving, in *ECS National Meeting Book of Abstract* (1967).
- [2] S. M. Irving, *Solid State Technology* **14**, 47 (1971).
- [3] H. Abe, Y. Sonobe, and T. Enomoto, *Jpn. J. Appl. Phys.* **12**, 154 (1973).
- [4] R. A. H. Heinecke, *Solid State Electron.* **18**, 1146 (1975).
- [5] R. A. H. Heinecke, *Solid State Electron.* **19**, 1039 (1976).
- [6] H. F. Winters and J. W. Coburn, *Appl. Phys. Lett.* **34**, 70 (1979).
- [7] V. M. Donnelly and A. Kornblit, *J. Vac. Sci. Technol. A* **31**, 050825 (2013).
- [8] W. B. Jung, S. Jang, S. Y. Cho, H. J. Jeon, and H. T. Jung, *Adv. Mater.* **32**, 1907101 (2020).
- [9] A. Pavlik, G. Marcos, M. Coulibaly, J. Vincent, T. Czerwiec, and S. Philippon, *Tribology International* **146**, 106232 (2020).
- [10] A. Lasagni, S. Alamri, A. Aguilar-Morales, F. Rosler, B. Voisiat, and T. Kunze, *Appl. Sci.* **8**, 1260 (2018).
- [11] P. Ge, S. Wang, J. Zhang, and B. Yang, *Materials Horizons* **7**, 2566 (2020).
- [12] J.-. Nilsson, *Can mankind survive without stainless steels ?*
- [13] F. A. P. Fernandes, L. C. Casteletti, G. E. Totten, and J. Gallego, *Int. Heat Treatment Surf. Eng.* **6**, 103 (2012).
- [14] C. E. Pinedo and A. Tschiptschin, *Rem Revista Escola de Minas* **66**, 209 (2013).
- [15] B. R. Kumar, S. Shairma, B. P. Kashyap, and N. Pabhu, *Materials and Design* **68**, 63 (2015).
- [16] N. Laegreid and G. K. Wehner, *J. Appl. Phys.* **32**, 365 (1961).
- [17] R. Behrisch and W. Eckstein, *Sputtering by Particle Bombardment* (2007), ISBN 978-3-540-44500-5.
- [18] N. D. Altieri, J. K.-C. Chen, L. Minardi, and J. P. Chang, *J. Vac. Sci. Technol. A* **35**, 05C203 (2017).
- [19] H. Jang, A. Efremov, J. S. Yunc, G. Y. Yeomd, and K.-H. Kime, K. B. Kwon, *Applied Surface Science* **279**, 41 (2013).
- [20] R. Ramos, *Interactions entre les plasmas de gravure a couplage inductif et les parois du reacteur*, Ph.D. thesis (2008).
- [21] J. Cunge, M. Kogelshatz, O. Joubert, and N. Sadeghi, *Plasmas Sources Sci. Technol.* **14**, S42 (2005).
- [22] C. Haag and H. Suhr, *Plasma Chem. Plasma P.* **6**, 197 (1986).
- [23] A. S. Orland and R. Blumenthal, *J. Vac. Sci. Technol. B* **23**, 1589 (2005).
- [24] A. S. Orland and R. Blumenthal, *J. Vac. Sci. Technol. B* **23**, 1597 (2005).
- [25] K.-C. Chen, *Generalized Approach for Selecting Plasma Chemistries in Metal Etch*, Ph.D. thesis (2016).
- [26] N. Altieri, *Atomic Layer Etching of Magnetic and Noble Metals*, Ph.D. thesis (2018).
- [27] V. M. Donnelly, M. V. Malyshev, A. Kornblit, N. A. Ciampa, J. I. Colonell, and J. T. C. Lee, *Jpn. J. Appl. Phys.* **37**, 2388 (1998).
- [28] V. M. Donnelly, *J. Phys. D: Appl. Phys.* **37**, R217 (2004).
- [29] N. C. M. Fuller, V. M. Donnelly, and I. P. Herman, *J. Vac. Sci. Technol. A* **20**, 170 (2002).
- [30] N. C. M. Fuller, I. P. Herman, and V. M. Donnelly, *J. Appl. Phys.* **90**, 3182 (2001).
- [31] M. V. Malyshev, V. M. Donnelly, A. Kornblit, and N. A. Ciampa, *J. Appl. Phys.* **84**, 137 (1998).
- [32] M. V. Malyshev and V. M. Donnelly, *Plasma Sources Sci. Technol.* **9**, 353 (2000).
- [33] A. Efremov, D.-P. Kim, and C.-I. Kim, *J. Vac. Sci. Technol. A* **21**, 1568 (2003).
- [34] A. M. Efremov, G.-H. Kim, J.-G. Kim, A. V. Bogomolov, and C.-I. Kim, *Microelectron. Eng.* **84**, 136 (2007).
- [35] R. Chanson, A. Rhallabi, M. C. Fernandez, , and C. Cardinaud, *Plasma Process. Polym.* **10**, 213 (2013).
- [36] H. Cho, K. B. Jung, D. C. Hays, Y. B. Hahn, E. S. Lambers, T. Feng, Y. D. Park, J. R. Childress, and S. J. Pearton, *Appl. Surf. Sci.* **140**, 215 (1998).
- [37] M. S. P. Andriese, E. van der Drift, and W. G. Sloof, *J. Vac. Sci. Technol. B* **19**, 2901 (2001).
- [38] H. J. Park, H.-W. Ra, K. S. Song, and Y.-B. Hahn, *Korean J. Chem. Eng.* **21**, 1235 (2004).

- [39] W. M. Haynes, D. R. Lide, and T. J. Bruno, *Handbook of Chemistry and Physics 97th Edition* (CRC Press, 2016), 97th ed., ISBN 978-1498754286.
- [40] B. B. Ebbinghaus, *Combust. Flame* **101**, 311 (1995).
- [41] B. Wu, *J. Vac. Sci. Technol. B* **24**, 1 (2006).
- [42] H. Abe, K. Nishioka, S. Tamura, and A. Nishimoto, *Jpn. J. Appl. Phys.* **15**, 25 (1976).
- [43] F. Aydinoglu, *J. Vac. Sci. Technol. B* **35**, 06GB01 (2017).
- [44] B. J. Curtis, H. R. Brunner, and M. Ebonether, *J. Electrochem. Soc.* **130**, 2242 (1983).
- [45] D. Staaks, X. M. Yang, K. Y. Lee, S. D. Dhuey, S. Sassolini, I. W. Rangelow, and D. L. Olynick, *Nanotechnology* **27**, 415302 (2016).
- [46] D. Staaks, Z. Yu, S. D. Dhuey, S. Sassolini, K. Y. Lee, I. W. Rangelow, and D. L. Olynick, *J. Vac. Sci. Technol. A* **37**, 061306 (2019).
- [47] H. Nakata, K. Nishioka, and H. Abe, *J. Vac. Sci. Technol.* **17**, 1351 (1980).
- [48] T. Ichiki, S. Takayanagi, and Y. Horiike, *J. Electrochem. Soc.* **147**, 4289 (2000).
- [49] S.-Y. Kang, K.-H. Kwon, K. S.-I., L. S.-K., M.-Y. Jung, Y.-R. Cho, Y.-H. Song, J. H. Lee, and K.-I. Cho, *J. Electrochem. Soc.* **148**, G237 (2001).
- [50] L. Lallement, A. Rhallabi, C. Cardinaud, and M. Fernandez, *J. Vac. Sci. Technol. A* **29**, 051304 (2011).
- [51] G. Le Dain, A. Rhallabi, M.-C. Fernandez, M. Boufnichel, and F. Roqueta, *J. Vac. Sci. Technol. A* **35**, 03E113 (2017).
- [52] M. Wang and M. J. Kushner, *J. Appl. Phys.* **107**, 023309 (2010).
- [53] V. Ishchuk, B. E. Volland, M. Hauguth, M. Cooke, and I. W. Rangelow, *J. Appl. Phys.* **112**, 084308 (2012).
- [54] G. Memos, E. Lidorikis, E. Gogolides, and G. Kokkoris, *J. Phys. D: Appl. Phys.* **54**, 175205 (2021).
- [55] C. Lee and M. Lieberman, *J. Vac. Sci. Technol.* **13**, 368 (1995).
- [56] A. Rhallabi and Y. Catherine, *IEEE Trans. Plasma Sci.* **19**(2), 270 (1991).
- [57] R. Chanson, A. Rhallabi, M. C. Fernandez, C. Cardinaud, S. Bouchoule, L. Gatilova, and A. Talneau, *IEEE Trans. Plasma Sci.* **40**, 959 (2012).
- [58] E. G. Thorsteinsson and J. T. Gudmundsson, *J. Phys. D: Appl. Phys.* **43**, 115201 (2010).
- [59] A. Efremov, J. Lee, and K.-H. Kwon, *Thin Solid Films* **629**, 39 (2017).
- [60] E. Kemaneci, E. Carbone, J.-P. Booth, W. Graef, J. van Dijk, and G. Kroesen, *Plasma Sources Sci. Technol.* **23**, 045002 (2014).
- [61] R. R. Hamilton, J. Tennyson, J.-P. Booth, T. Gans, and A. R. Gibson, *Plasma Sources Sci. Technol.* **27**, 095008 (2018).
- [62] M.-W. Ruf, S. Barsotti, M. Braun, H. Hotop, and I. I. Fabrikant, *J. Phys. B: At. Mol. Opt. Phys.* **37**, 41 (2004).
- [63] R. Basner and K. Becker, *New J. Phys.* **6**, 118 (2004).
- [64] A. M. Ali and Y.-K. Kim, *Surf. Interface Anal.* **37**, 969 (2005).
- [65] P. Calandra, C. S. S. O'Conno, and S. D. Price, *J. Chem. Phys.* **112**, 10821 (2000).
- [66] K. Fritioff, J. Sandstrom, D. Hanstorp, A. Ehlerding, M. Larsson, G. F. Collins, D. J. Pegg, A. Danared, H. Kallberg, and A. Le Padellec, *Phys. Rev. A* **68**, 012712 (2003).
- [67] D. Burgess, M. Zachariah, W. Tsang, and P. Westmoreland, *Prog. Energy Combust. Sci.* **21**, 453 (1995).
- [68] V. M. Donnelly and M. V. Malyshev, *Appl. Phys. Lett.* **77**, 2467 (2000).
- [69] E. G. Thorsteinsson and J. T. Gudmundsson, *Plasma Sources Sci. Technol.* **19**, 055008 (2010).
- [70] N. Singh, A. K. S. Jha, and M. Mohan, *Eur. Phys. J. D* **38**, 285 (2006).
- [71] P. Chantry, *J. Appl. Phys.* **62**, 1141 (1987).
- [72] G. P. Kota, J. W. Coburn, and D. B. Graves, *J. Vac. Sci. Technol. A* **17**, 282 (1999).
- [73] G. Cartry, X. Duten, and A. Rousseau, *Plasma Sources Sci. Technol.* **15**, 479 (2006).
- [74] A. Manenschijn, G. C. A. M. Janssen, E. van der Drift, and S. Radelaar, *J. Appl. Phys.* **69**(3), 1253 (1991).

- [75] Y. Haidar, A. Pateau, A. Rhallabi, M. C. Fernandez, A. Mokrani, F. Taher, F. Roqueta, and M. Boufnichel, *Plasma Sources Sci. Technol.* **23**, 065037 (2014).
- [76] G. Kokkoris, A. Goodyear, M. Cooke, and E. Gogolides, *J. Phys. D: Appl. Phys.* **41**(19), 195211 (2008).
- [77] G. Marcos, A. Rhallabi, and P. Ranson, *J. Vac. Sci. Technol. A* **21**(1), 87 (2003).
- [78] G. Marcos, A. Rhallabi, and P. Ranson, *Mat. Res. Soc. Symp. Proc.* **782**, A5.78.1 (2003).
- [79] G. Le Dain, A. Rhallabi, C. Cardinaud, A. Girard, M.-C. Fernandez, M. Boufnichel, and F. Roqueta, *J. Vac. Sci. Technol. A* **36**, 03E109 (2018).
- [80] A. K. Srivastava, T. Ohashi, and V. M. Donnelly, *J. Vac. Sci. Technol. A* **33**, 041301 (2015).
- [81] J. F. Ziegler, M. D. Ziegler, and J. P. Biersack, *Nucl. Instrum. Meth. B* **268**, 1818 (2010).
- [82] G. Kokkoris, V. Constantoudis, P. Angelikopoulos, G. Boulousis, and E. Gogolides, *Phys. Rev. B* **76**, 193405 (2007).
- [83] G. Kokkoris and E. Gogolides, *J. Phys. D: Appl. Phys.* **45**, 165204 (2012).
- [84] C. Cardinaud, M. Peignon, and P. Tessier, *Appl. Surf. Sci.* **164**, 72 (2000).
- [85] T. Meyer, A. Girard, G. Le Dain, A. Rhallabi, E. Baudet, P. Nazabal, V. Nemeč, and C. Cardinaud, *Appl. Surf. Sci.* **549**, 149192 (2021).
- [86] G. Herzberg, *Molecular Spectra & Molecular Structure : Electronic Spectra and Electronic Structure of Polyatomic Molecules* (1991), 2nd ed.
- [87] R. W. B. Pearse and A. G. Gaydon, *The Identification of Molecular Spectra* (1976), 4th ed.
- [88] H. Hutchinson, *Principles of plasma diagnostics* (Cambridge University Press), 1st ed., ISBN 978-0521326223.
- [89] M. V. Malyshev and V. M. Donnelly, *J. Appl. Phys.* **88**, 6207 (2000).
- [90] J. W. Coburn and H. F. Winters, *J. Vac. Sci. Technol.* **16**(2), 391 (1979).
- [91] M. V. Malyshev, V. M. Donnelly, and S. Samukawa, *J. Appl. Phys.* **84**, 1222 (1998).
- [92] R. D. Bach, D. Shobe, and H. B. Schlegel, *J. Phys. Chem.* **100**, 8770 (1996).
- [93] G. Le Dain, A. Rhallabi, A. Girard, C. Cardinaud, F. Roqueta, and M. Boufnichel, *Plasma Sources Sci. Technol.* **28**, 085002 (2019).
- [94] T. Sasaki, K. Matsuda, M. Omura, I. Sakai, and H. Hayashi, *Jpn. J. Appl. Phys.* **54**, 06GB03 (2015).
- [95] D. Metzler, S. Engelmann, R. L. Bruce, E. A. Joseph, and G. S. Oehrlein, *J. Vac. Sci. Technol. A* **32**, 020603 (2014).
- [96] E. Laudrei, T. Tillocher, Y. Meric, P. Lefauchaux, B. Boutaud, and R. Dussart, *J. Micromech. Microeng.* **28**, 055010 (2018).
- [97] J. Lohani, S. Varshney, D. S. Rawal, S. Sapraa, and R. Tyagi, *Nano-Struct. Nano-Objects* **18**, 100284 (2019).
- [98] C. L. Yaws, *The Yaws Handbook of Vapor Pressure* (2015), 2nd ed., ISBN 978-0-12-802999-2.
- [99] L. Christophorou and J. Olthoff, *Fundamental Electron Interactions with Plasma Processing Gases*, vol. 1 (Springer US, 2004), 1st ed., ISBN 978-1-4419-8971-0.
- [100] M. V. Kurepa and D. S. Belic, *J. Phys. B: At. Mol. Opt. Phys.* **11**, 3719 (1978).
- [101] R. Chanson, *Gravure de l InP par plasma ICP chlore et HBr/Ar : Modelisation multiechelle et analyse XPS*, Ph.D. thesis, University of Nantes (2012).
- [102] E. Despiau-Pujo, M. Brihoum, P. Bodart, M. Darnon, and G. Cunge, *J. Phys. D: Appl. Phys.* **47**, 455201 (2014).
- [103] P. S. Ganas, *J. Appl. Phys.* **63**, 277 (1988).

Table 1. Plasma-surface reactions between neutral superparticles and supersites. (g) sign correspond to gaseous species and (s) sign to solid or surface species. P_{des} is a probability specific to each supersite and evolves with ion bombardment, its evolution is explained in table 2. Redeposition neutrals are sputtered sites.

Reaction	Probability	Probability
Chemical etching with neutrals	Initial	After ion bombardment
$Cl(g) + FeCl_x(x = 0 - 1)(s) \rightarrow FeCl_{x+1}(s)$	0.05	$0.05 + P_{des}$
$Cl(g) + FeCl_2(s) \rightarrow FeCl_3(g)$	0.05	$0.05 + P_{des}$
$Cl(g) + CrCl_x(x = 0 - 1)(s) \rightarrow CrCl_{x+1}(s)$	0.05	$0.05 + P_{des}$
Neutrals redeposition	Initial	After ion bombardment
$FeCl_x(g) + Surface \rightarrow FeCl_x(x = 0 - 2)(s)$	0.1	$0.1 + P_{des}$
$CrCl_x(g) + Surface \rightarrow CrCl_x(x = 0 - 2)(s)$	0.1	$0.1 + P_{des}$
$SiO_2(g) + Surface \rightarrow SiO_2(s)$	0.1	$0.1 + P_{des}$

Table 2. Plasma-surface reactions between ionic superparticles and supersites. (g) sign correspond to gaseous species and (s) sign to solid or surface species. SY means Sputtering Yield, it is the sputtering yield calculated by SRIM. E is the ion energy, A is the incident angle of ion with respect to the surface normal. Spontaneous desorption appears after ion/surface interaction. As an example, a Fe site with two sputtered neighbours has a desorption probability of 0.08. Cl_2^+ has the same sputtering yield than Cl^+ as a first approximation.

Physical etching with ions	
Reaction	Yield
$(Cl^+, Cl_2^+) + FeCl_x(x = 0 - 2)(s) \rightarrow FeCl_x(x = 0 - 2)(g)$	$SY_{Cl^+ \rightarrow Fe}((E_{Cl^+}(eV), A_{Cl^+}(\circ)))$
$(Cl^+, Cl_2^+) + CrCl_x(x = 0 - 1)(s) \rightarrow CrCl_x(x = 0 - 2)(g)$	$SY_{Cl^+ \rightarrow Cr}((E_{Cl^+}(eV), A_{Cl^+}(\circ)))$
$(Ar^+) + FeCl_x(x = 0 - 2)(s) \rightarrow FeCl_x(x = 0 - 2)(g)$	$SY_{Ar^+ \rightarrow Fe}((E_{Ar^+}(eV), A_{Ar^+}(\circ)))$
$(Ar^+) + CrCl_x(x = 0 - 1)(s) \rightarrow CrCl_x(x = 0 - 2)(g)$	$SY_{Ar^+ \rightarrow Cr}((E_{Ar^+}(eV), A_{Ar^+}(\circ)))$
Physical etching with ions hard areas	
Reaction	Yield
$(Cl^+, Cl_2^+) + FeCl_x(x = 0 - 2)(s) \rightarrow FeCl_x(x = 0 - 2)(g)$	$SY/5$
$(Cl^+, Cl_2^+) + CrCl_x(x = 0 - 1)(s) \rightarrow CrCl_x(x = 0 - 2)(g)$	$SY/5$
$(Ar^+) + FeCl_x(x = 0 - 2)(s) \rightarrow FeCl_x(x = 0 - 2)(g)$	$SY/5$
$(Ar^+) + CrCl_x(x = 0 - 1)(s) \rightarrow CrCl_x(x = 0 - 2)(g)$	$SY/5$
Spontaneous desorption (Initial $P_{des} = 0$)	
Interaction site	Interaction site hard areas
$P_{des} = P_{des} + 0.1$	$P_{des} = P_{des} + 0.05$
1^{st} neighbours	1^{st} neighbours hard areas
$P_{des} = P_{des} + 0.04$	$P_{des} = P_{des} + 0.002$

List of Figures

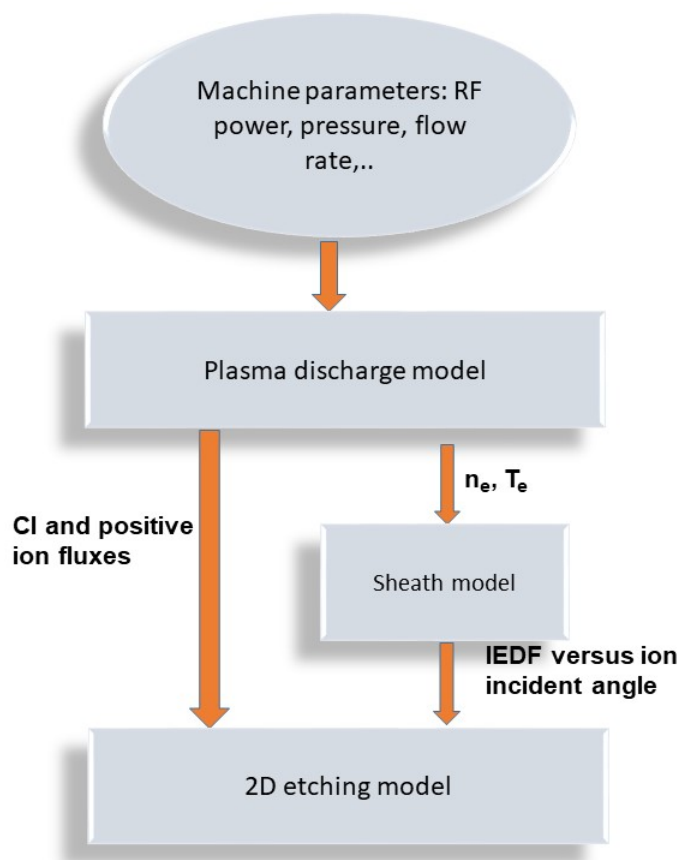


Figure 1. Flowchart of model. The total simulation range applied for conditions close to those presented in table 3, in terms of power, pressure, flow rate, bias and etching duration. In the conditions applied for this paper, total simulation time is about 1-2 hours, simulation time of each model is around 30 minutes. Spatial scale of sheath model is sheath length, so around 1mm while spatial scale of surface model is $1\mu\text{m}$ for the feature.

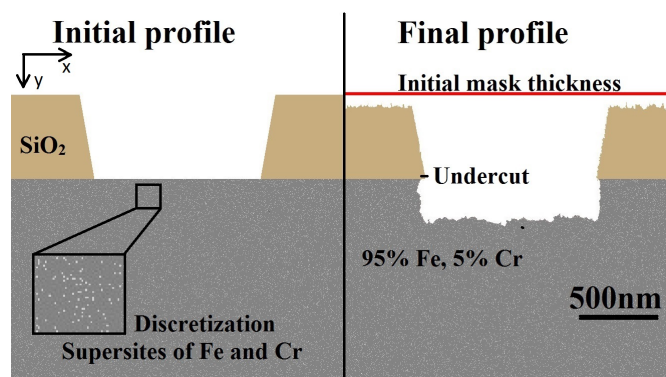


Figure 2. Initial and final profile provided by surface model during Fe/Cr etching using pure Cl_2 plasma.

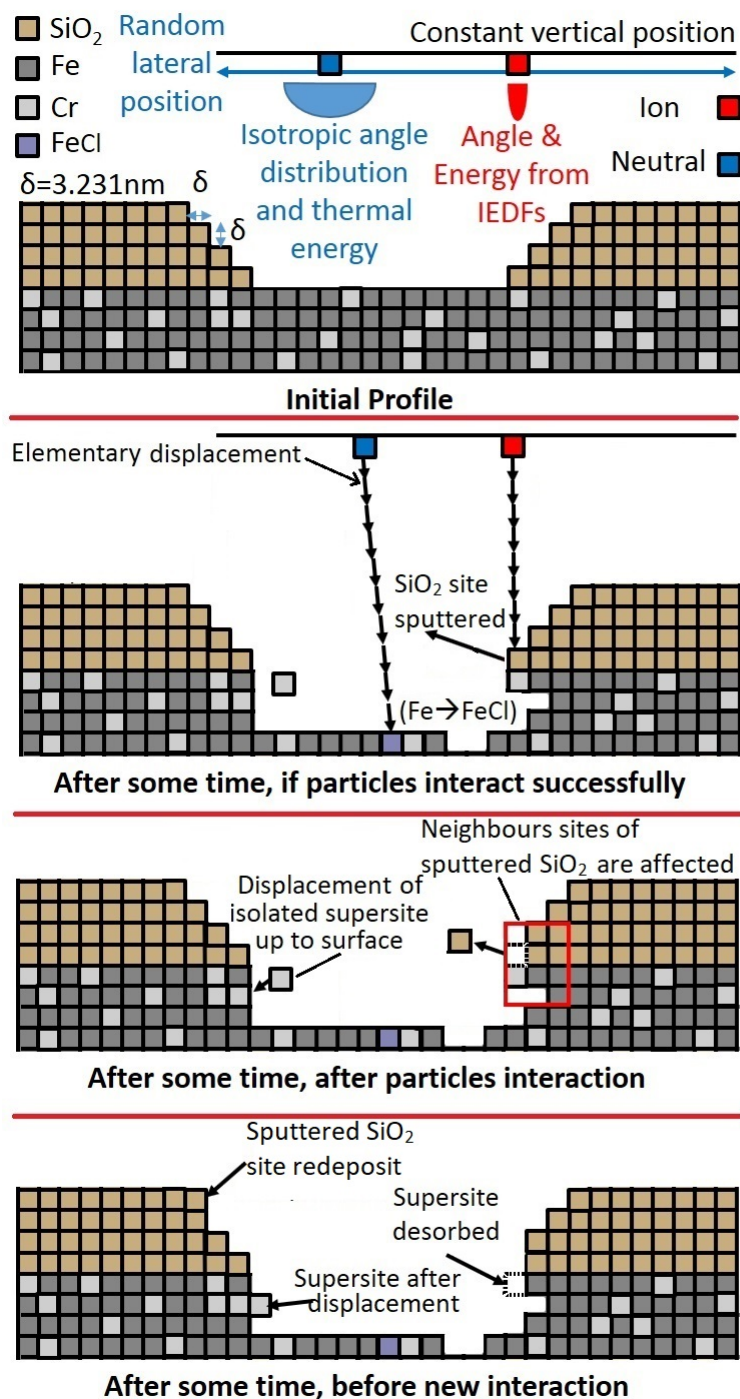


Figure 3. Description of successful treatment for superparticle-surface interaction. Only one superparticle (neutral or ion) interact at the same time. Redeposition, modification of desorption probability are treated after and finally diffusion. Neighbours affected by sputtering is ion enhanced etching, which is described in section 3 Displacement there concerns the displacement of surface supersites until they reach surface, they are not going into the substrate. It is a security procedure implemented to avoid the creation of voids between surface supersites and surface, which is not physically relevant. After three adsorptions of *Cl* on the same site, *Fe* becomes *FeCl*₃ disappears because it is gaseous.

Table 3. Experimental conditions for etching plasmas in ICP/RIE SENTECH reactor. %wt of *Cr* into *Fe – Cr* alloys are 0, 1, 3, 5, 8 and 12.

Substrate	<i>Fe</i> or <i>Cr</i>	<i>Fe – Cr</i> alloys
Power(<i>W</i>)	800	800
Pressure(<i>mTorr</i>)	5	5
Flow rate <i>Cl</i> ₂ (<i>sccm</i>)	60	60
Flow rate <i>Ar</i> (<i>sccm</i>)	60	0
Bias (<i>V</i>)	-150	-150
Surface temperature (<i>°C</i>)	150 or 220	220
Duration (<i>min</i>)	2	2

Table 4. Experimental conditions for the cleaning procedure of the ICP/RIE SENTECH.

Step	1	2	3
Flow rate <i>Cl</i> ₂ (<i>sccm</i>)	20	0	0
Flow rate <i>Ar</i> (<i>sccm</i>)	10	0	40
Flow rate <i>O</i> ₂ (<i>sccm</i>)	0	40	0
Pressure (<i>mTorr</i>)	3	3	3
ICP RF Power (<i>W</i>)	500	500	300
Temperature (<i>°C</i>)	20	20	20
Duration (<i>min</i>)	20	15	5

Table 5. Etch rates in *nm/min* of iron and chromium estimated by experiment, conditions are presented in table 3.

Sample	<i>Cl</i> ₂	<i>Ar</i>
Iron	269(±5)	40 (±1)
Chromium	45 (±3)	26 (±2)

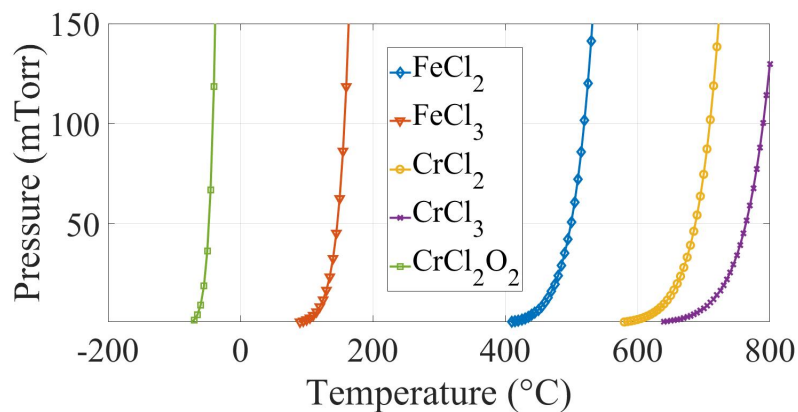


Figure 4. Vapor pressure of chlorinated metals from Yaws handbook [98].

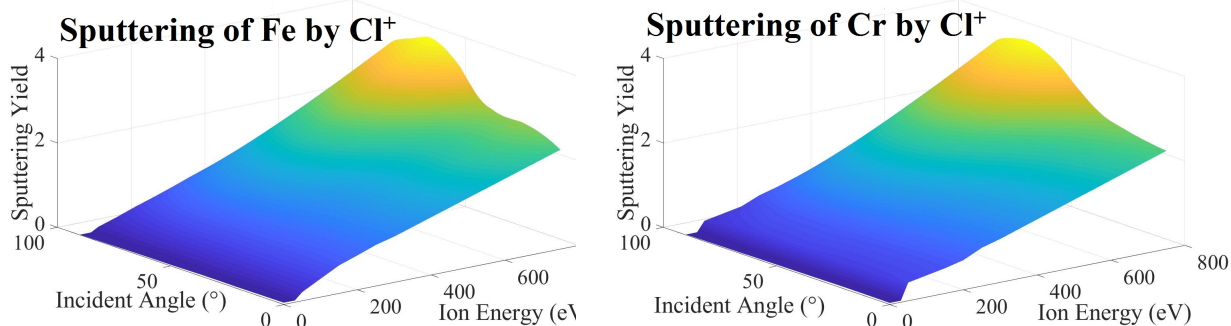


Figure 5. Sputtering yields of elements by Cl^+ ions, calculated using *SRIM*© software for different energy and incident angles.

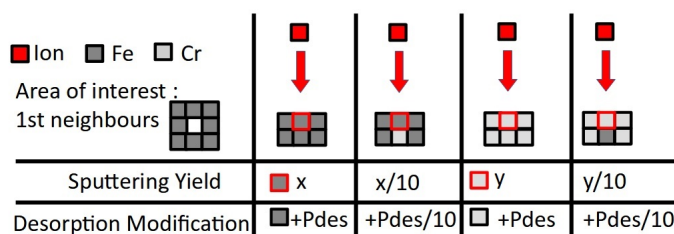


Figure 6. Drawing of the numerical treatment of hard zones and its implications. The supersite surrounded by red is the interaction supersite. Modification of desorption probability concerns the neighbours of the interaction supersite and itself. Area of interest is the area explored to research iron or chromium presence.

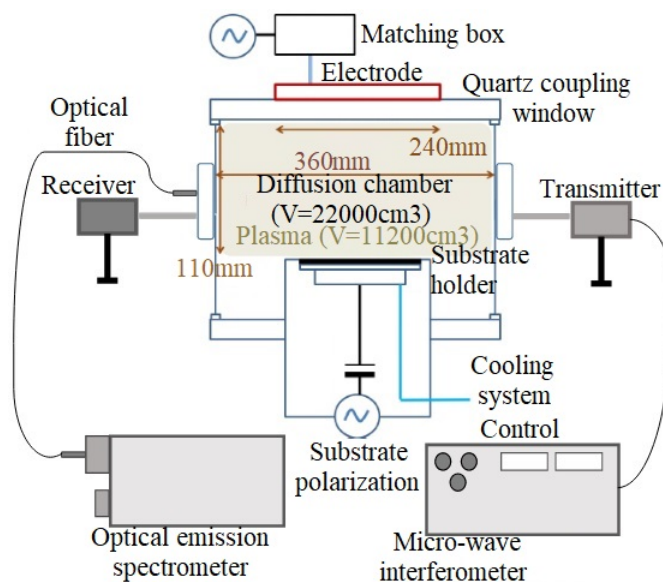


Figure 7. Drawing of an ICP/RIE SENTECH reactor SI500 with interferometer and optical emission spectroscopy tools implemented.

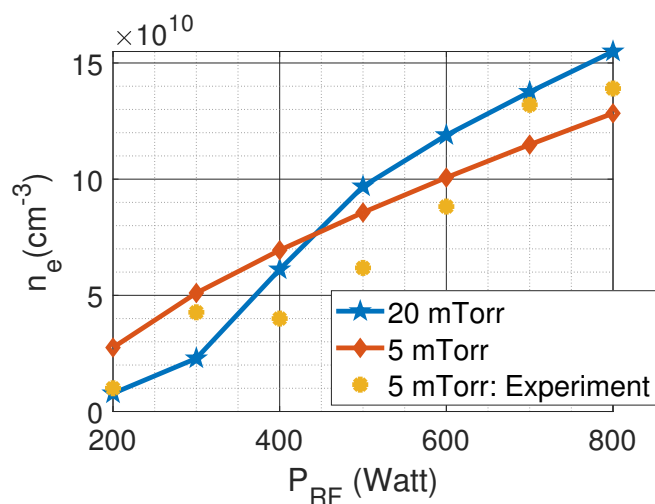


Figure 8. Electron density evolution versus RF power for two different pressures and for initial conditions presented in table 3, with neither metallic substrate nor bias.

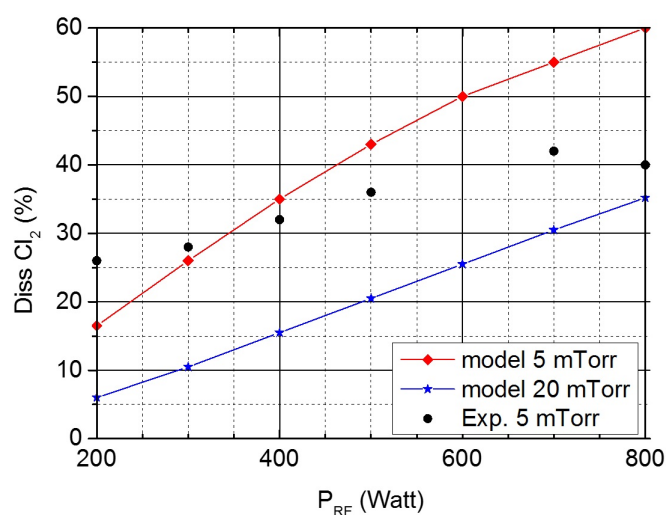


Figure 9. Dissociation percentage versus RF power for two different pressures and for initial conditions presented in table 3, with neither metallic substrate nor bias. Note that dissociation percentage is not estimated the same way for experiment and for simulation. Simulation data use the evolution of $(1 - n_{Cl_2}(plasma_{on}))/n_{Cl_2}(plasma_{off})$ ratio while experimental data use I_{Cl}/I_{Xe} ratio to estimate the dissociation percentage. I_{Cl}/I_{Xe} is multiplied by a constant value of 20 for each points for graphical scaling purpose. Only trends can be compared and not absolute values.

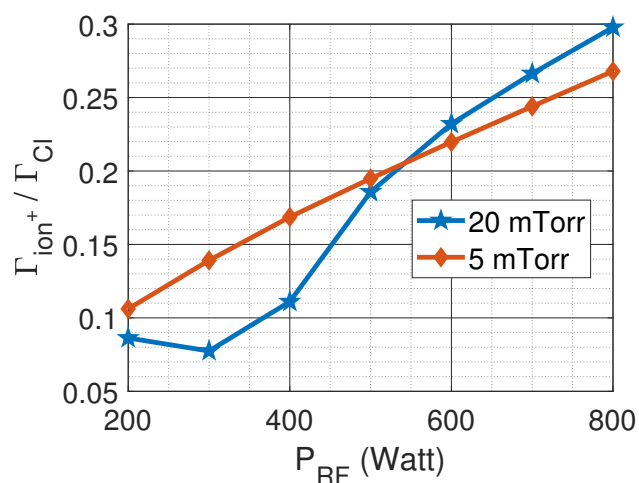


Figure 10. Ion to neutral flux ratio versus RF power for initial conditions presented in table 3 without substrate and without bias.

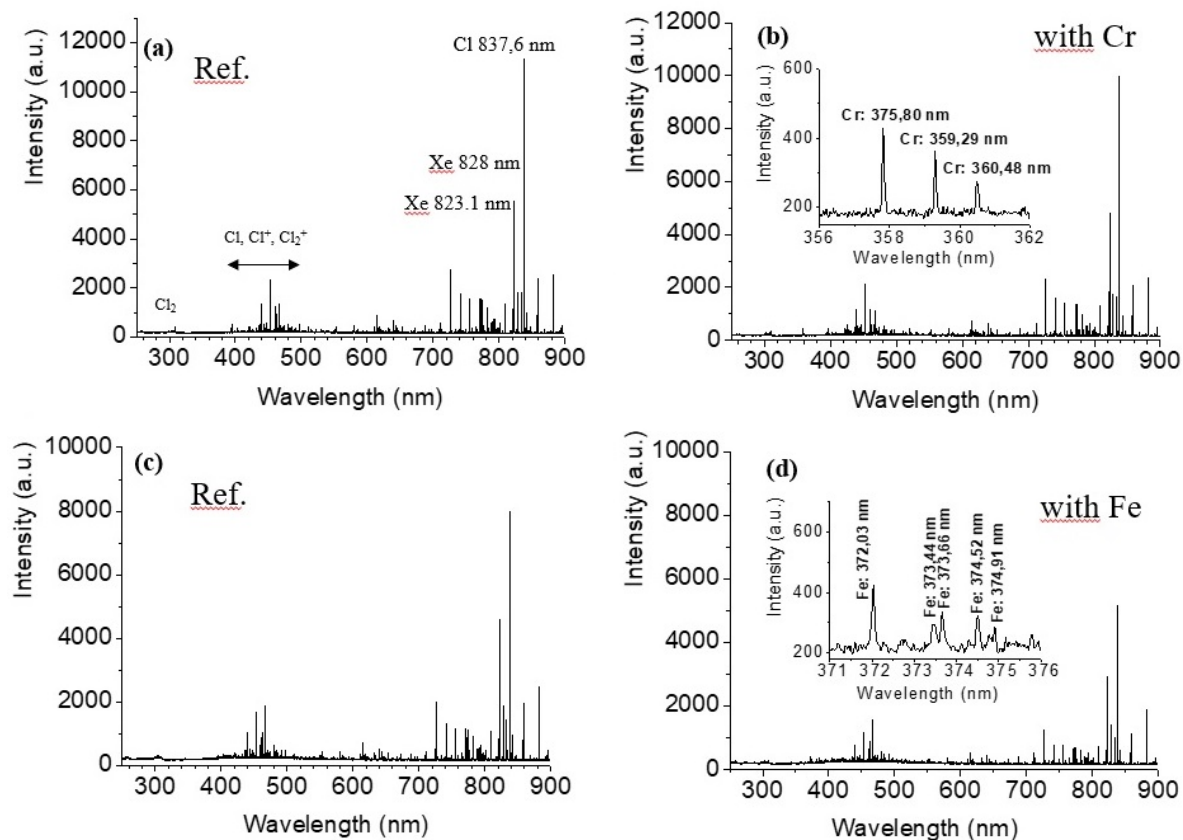


Figure 11. Emission spectra of a chlorine plasma. Pressure is 5 mTorr, RF Power is 800 W, Cl_2 flow rate is 60 sccm Xe flow rate is 7 sccm with neither bias, nor substrate heating. There is a Cr metallic substrate for figure b and a Fe metallic substrate for figure d.

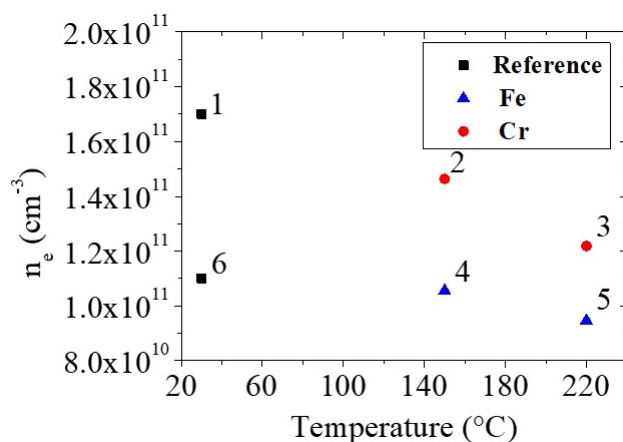


Figure 12. Electron density of Cl_2 plasmas for conditions presented in table 3 with different substrate temperatures ($150\text{ }^\circ C$ for points 2 and 4, $220\text{ }^\circ C$ for points 3 and 5). References of n_e given by points 1 and 6 (without substrate heating), before any etching (point 1) and after every etching (point 6).

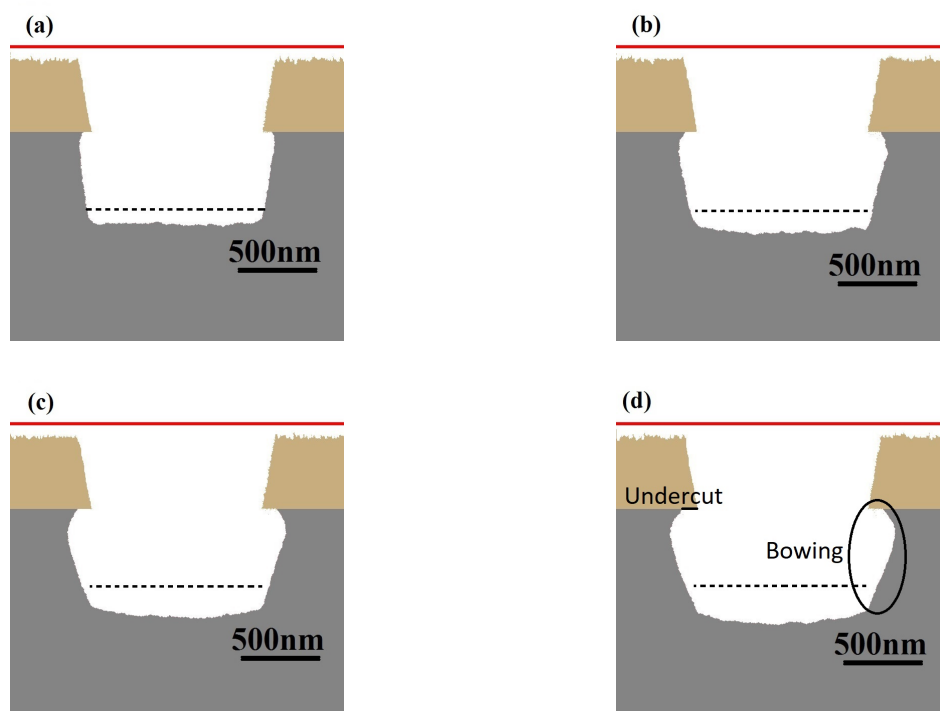


Figure 13. Trenches profiles determined by modeling for different reflection probability for $Cl \rightarrow FeCl_x$ ($x = 0 - 2$) reactions : (a) $P_{ads} = 0.1$, (b) $P_{ads} = 0.2$, (c) $P_{ads} = 0.3$ and (d) $P_{ads} = 0.4$. Etching time is 2 min , other operating conditions are presented in table 3. Dashed lines represent etching depth estimated with experimental etch rate for pure iron sample.

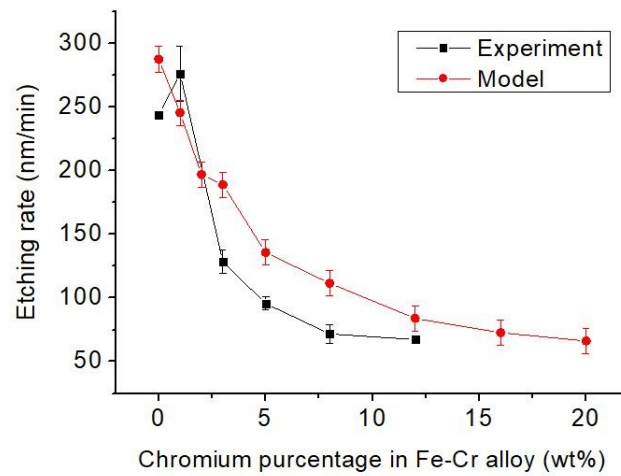


Figure 14. Experimental and modeling etch rates of Fe/Cr target with different $\%Cr$. Operating conditions are presented in table 3.

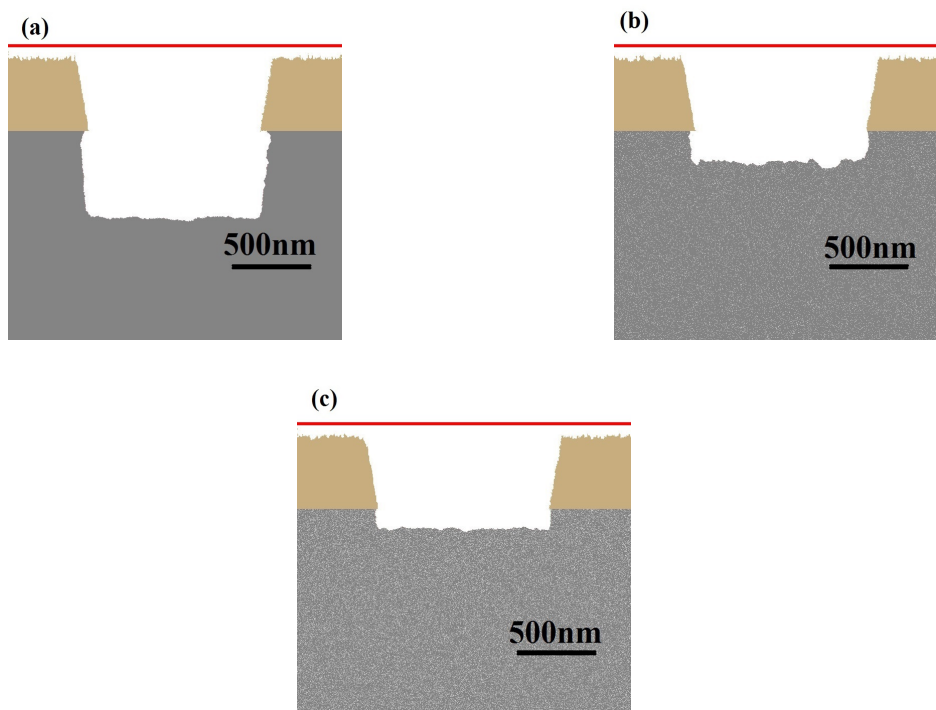


Figure 15. Trenches profiles determined by modeling for : (a) 0 %wt Cr , (b) 8%wt Cr and (c) 20%wt Cr . Etching time is 2 min, other operating conditions are presented in table 3

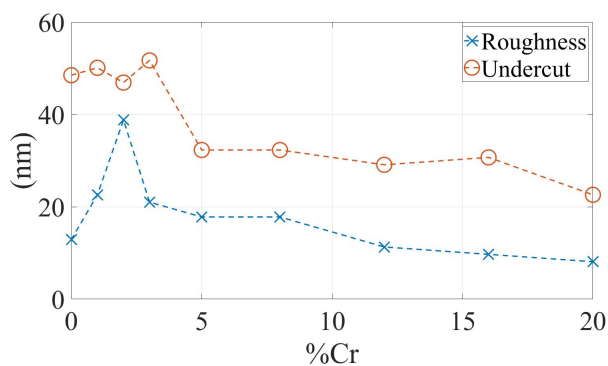


Figure 16. Roughness and undercut measured of Fe/Cr targets, from model results with different $\%wt Cr$. Operating conditions are presented in table 3.

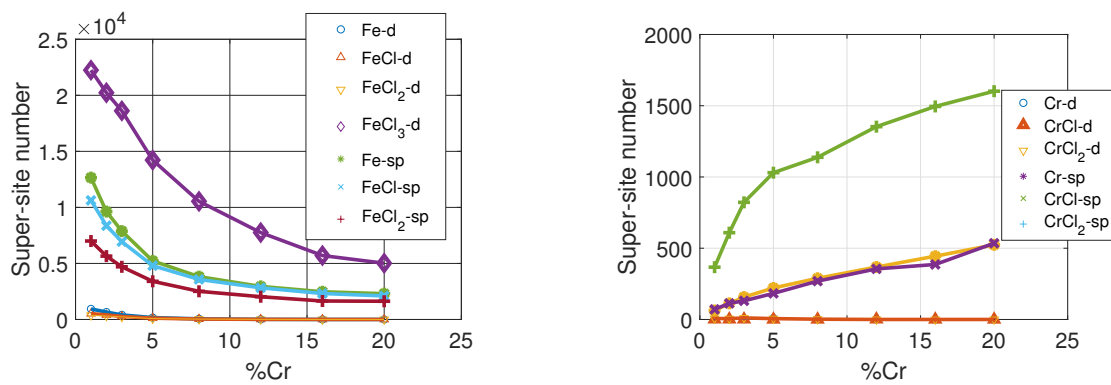


Figure 17. Number of supersites etched by different processes for Fe/Cr targets. Iron case is presented in (a), while chromium is presented in (b). From model results with different $\%Cr$ or $\%Fe$. Operating conditions are presented on table 3. d sign corresponds to desorption while sp sign corresponds to sputtering.

Table 6. Species taken into account for pure Cl_2 plasma. $Cl_2(A, C)$ corresponds to $a^3\Pi_u, A^1\Pi_u, b^3\Pi_g, c^3\Sigma_g^-$ et $B^1\Pi_g$ states. $Cl_2(B)$ corresponds to $C^1\Delta_g, D^1\Sigma_g^+$ et $e^3\Sigma_u^+$ states.

	Neutrals	Positive Ions	Negative Ions
	$Cl_2(\nu = 0 - 1 - 2 - 3), Cl_2(A, C), Cl_2(B), Cl, Cl(4s), Cl(4p), Cl(3d)$	Cl_2^+, Cl^+	Cl^-

Table 7. Reactions of dissociation and ionization for Cl_2 plasma

Reaction	Threshold Energy (eV)	Reaction rate ($cm^3.s^{-1}$)	ref
$R_1 : e + Cl_2(\nu = 0 - 3) \rightarrow 2Cl + e$	0.0	$k_4 = 6.67 \times 10^{-8} Te^{-0.1} exp(-8.67/Te)$	[99, 61]
$R_2 : e + Cl_2(\nu = 0 - 3) \rightarrow Cl_2(a^3\Pi_u) + e \rightarrow Cl_2(A, C) + e$	3.252	$k_{13} = 8.0 \times 10^{-8} Te^{-0.55} exp(-5.5/Te)$	[99, 61]
$R_3 : e + Cl_2(\nu = 0 - 3) \rightarrow Cl_2(A^1\Pi_u) + e \rightarrow Cl_2(A, C) + e$	4.348	$k_{14} = 1.0 \times 10^{-7} Te^{-0.675} exp(-7.0/Te)$	[99, 61]
$R_4 : e + Cl_2(\nu = 0 - 3) \rightarrow Cl_2(b^3\Pi_g) + e \rightarrow Cl_2(A, C) + e$	6.498	$k_{20} = 4.0 \times 10^{-8} Te^{-0.6} exp(-10.2/Te)$	[99, 61]
$R_5 : e + Cl_2(\nu = 0 - 3) \rightarrow Cl_2(c^3\Sigma_g^-) + e \rightarrow Cl_2(A, C) + e$	7.257	$k_{26} = 2.0 \times 10^{-10} Te^{-0.6} exp(-9.0/Te)$	[99, 61]
$R_6 : e + Cl_2(\nu = 0 - 3) \rightarrow Cl_2(B^1\Pi_g) + e \rightarrow Cl_2(A, C) + e$	7.537	$k_{15} = 3.0 \times 10^{-9} Te^{-0.5} exp(-11.0/Te)$	[99, 61]
$R_7 : e + Cl_2(\nu = 0 - 3) \rightarrow Cl_2(C^1\Delta_g) + e \rightarrow Cl_2(B) + e$	7.790	$k_{27} = 5.0 \times 10^{-10} Te^{-0.6} exp(-10.0/Te)$	[99, 61]
$R_8 : e + Cl_2(\nu = 0 - 3) \rightarrow Cl_2(D^1\Sigma_g^+) + e \rightarrow Cl_2(B) + e$	8.228	$k_{16} = 5.0 \times 10^{-10} Te^{-0.75} exp(-12.0/Te)$	[99, 61]
$R_9 : e + Cl_2(\nu = 0 - 3) \rightarrow Cl_2(e^3\Sigma_u^+) + e \rightarrow Cl_2(B) + e$	9.219	$k_{17} = 1.0 \times 10^{-10} Te^{-0.5} exp(-11.0/Te)$	[99, 61]
$R_{10} : e + Cl_2(\nu = 0 - 3) \rightarrow Cl_2(^2\Sigma_u^+) \rightarrow Cl + Cl^-$	0.0	$k_{51} = 6.5 \times 10^{-11} Te^{-1.4} exp(-0.0/Te)$	[62, 100, 99]
$R_{11} : e + Cl_2(\nu = 0 - 3) \rightarrow Cl_2(^2\Pi_g)^- \rightarrow Cl + Cl^-$	2.5	$k_{52} = 5.5 \times 10^{-10} Te^{-1.3} exp(-2.0/Te)$	[62, 100, 99]
$R_{12} : e + Cl_2(\nu = 0 - 3) \rightarrow Cl_2(^2\Pi_u)^- \rightarrow Cl + Cl^-$	5.5	$k_{53} = 3.15 \times 10^{-9} Te^{-1.4} exp(-5.0/Te)$	[62, 100, 99]
$R_{13} : e + Cl_2 \rightarrow Cl + Cl^+ + 2e$	12.0	$k_2 = 2.14 \times 10^{-7} Te^{-0.07} exp(-25.26/Te)$	[65, 99, 63, 58, 60, 101]
$R_{14} : e + Cl_2 \rightarrow Cl^+ + Cl^- + e$	12.0	$k_3 = 2.94 \times 10^{-10} Te^{0.19} exp(-18.79/Te)$	[99, 62, 58, 60, 101]
$R_{15} : e + Cl_2 \rightarrow Cl_2^{2+} + 3e \rightarrow Cl^+ + Cl^+ + 3e$	35.0	$k_{50} = 2.27 \times 10^{-10} Te^{1.92} exp(-21.26/Te)$	[65, 99, 63, 58, 60]
$R_{16} : e + Cl_2 \rightarrow Cl_2^+ + 2e$	11.5	$k_1 = 5.12 \times 10^{-8} Te^{0.48} exp(-12.34/Te)$	[99, 63, 58, 60]
$R_{17} : e + Cl \rightarrow Cl^+ + 2e$	13.5	$k_6 = 3.17 \times 10^{-8} Te^{0.53} exp(-13.29/Te)$	[64, 58, 60, 101]

7. Annex

In this section, we present the full reaction scheme taken into account by the model, modified from Chanson *et al.* [57]. Reactions are presented as follow :

- Reactions of dissociation and ionization by electron impact in table 7;
- Reactions between charged species, atoms and molecules in table 8;
- Reactions of excitation and desexcitation in table 9;
- Surface reactions in table 10.
- Reactions concerning Ar in table 12.

Table 8. Reactions between charged species, atoms and molecules for Cl_2

Reaction	Threshold Energy (eV)	Reaction rate ($cm^3.s^{-1}$)	ref
Reactions electron-ion			
$R_{18} : e + Cl_2^+ \rightarrow 2Cl$	0.0	$k_{34} = 9.0 \times 10^{-8} T e^{-0.5}$	[101, 58, 60]
$R_{19} : e + Cl^- \rightarrow Cl + 2e$	10.1	$k_9 = 9.02 \times 10^{-9} T e^{0.72} \exp(-4.88/Te)$	[66, 101, 58, 60]
$R_{20} : e + Cl^- \rightarrow Cl^+ + 3e$	28.6	$k_{51} = 3.62 \times 10^{-9} T e^{0.72} \exp(-25.38/Te)$	[66, 101, 58, 60]
Reactions neutral-ion			
$R_{21} : Cl_2 + Cl^+ \rightarrow Cl_2^+ + Cl$	0.0	$k_{35} = 5.4 \times 10^{-10}$	[101, 58, 60]
Réactions neutre-neutre			
$R_{22} : Cl_2 + 2Cl \rightarrow 2Cl_2$	0.0	$k_{52} = 3.5 \times 10^{-27} \exp(810/T_{gaz})$	[58, 60]
$R_{23} : 2Cl + Cl \rightarrow Cl_2 + Cl$	0.0	$k_{53} = 8.75 \times 10^{-28} \exp(810/T_{gaz})$	[58, 60]
Reactions ion-ion, X is non chlorinated specie			
$R_{24} : Cl^- + Cl_2^+ \rightarrow Cl_2 + Cl$	0.0	$k_7 = 5.0 \times 10^{-8} (300/T_{gaz})^{0.5}$	[101, 58, 60]
$R_{25} : Cl^- + Cl^+ \rightarrow Cl + Cl$	0.0	$k_8 = 5.0 \times 10^{-8} (300/T_{gaz})^{0.5}$	[101, 58, 60]
$R_{26} : Cl_2^+ + Cl^- \rightarrow 3Cl$	0.0	$k_{54} = 5.0 \times 10^{-8} (300/T_{gaz})^{0.5}$	[102, 60]
$R_{27} : X^+ + Cl^- \rightarrow X + Cl$	0.0	$k_{55} = 5.0 \times 10^{-8} (300/T_{gaz})^{0.5}$	[59]

Table 9. Excitation and desexcitation reactions for Cl_2 .

Reaction	Threshold Energy (eV)	Reaction rate ($\text{cm}^3.\text{s}^{-1}$)	ref
Vibrational excitation			
$R_{28} : e + Cl_2(\nu = 0) \rightarrow Cl_2(\nu = 1) + e$	0.07	$k_{36} = 4.35 \times 10^{-10} T e^{-1.48} \exp(-0.76/Te)$	[101, 58, 60]
$R_{29} : e + Cl_2(\nu = 0) \rightarrow Cl_2(\nu = 2) + e$	0.14	$k_{37} = 8.10 \times 10^{-11} T e^{-1.48} \exp(-0.68/Te)$	[101, 58, 60]
$R_{30} : e + Cl_2(\nu = 0) \rightarrow Cl_2(\nu = 3) + e$	0.21	$k_{38} = 2.39 \times 10^{-11} T e^{-1.49} \exp(-0.64/Te)$	[101, 58, 60]
$R_{31} : e + Cl_2(\nu = 1) \rightarrow Cl_2(\nu = 2) + e$	0.07	$k_{31} = 1.04 \times 10^{-9} T e^{-1.48} \exp(-0.73/Te)$	[101, 58, 60]
$R_{32} : e + Cl_2(\nu = 1) \rightarrow Cl_2(\nu = 3) + e$	0.14	$k_{32} = 2.98 \times 10^{-10} T e^{-1.48} \exp(-0.67/Te)$	[101, 58, 60]
$R_{33} : e + Cl_2(\nu = 2) \rightarrow Cl_2(\nu = 3) + e$	0.07	$k_{33} = 1.04 \times 10^{-10} T e^{-1.48} \exp(-0.73/Te)$	[101, 58, 60]
$R_{34} : e + Cl_2(\nu = 0 - 3) \rightarrow Cl_2(\nu = 0 - 3) + e$	0.0	$k_{21} = 9.24 \times 10^{-9} \exp(-11.15/Te)$	[101, 58, 60]
Excitation by electronic impact			
$R_{35} : e + Cl \rightarrow Cl(4s) + e$	9.1	$k_{25} = 2.0 \times 10^{-8} \exp(-10.5/Te)$	[103, 101, 58, 60, 102]
$R_{36} : e + Cl \rightarrow Cl(4p) + e$	10.5	$k_{24} = 3.0 \times 10^{-8} \exp(-8.0/Te)$	[103, 101, 58, 60, 102]
$R_{37} : e + Cl \rightarrow Cl(3d) + e$	11.2	$k_{22} = 2.0 \times 10^{-8} \exp(-11.0/Te)$	[103, 101, 58, 60, 102]
$R_{38} : e + Cl \rightarrow Cl(5s) + e$	11.4	$k_{56} = 4.0 \times 10^{-9} \exp(-11.5/Te)$	[103, 102]
$R_{39} : e + Cl \rightarrow Cl(5p) + e$	11.8	$k_{57} = 1.5 \times 10^{-8} \exp(-11.77/Te)$	[103, 101, 58, 60, 102]
$R_{40} : e + Cl \rightarrow Cl(4d) + e$	12.0	$k_{23} = 1.27 \times 10^{-8} \exp(-12.0/Te)$	[103, 101, 58, 60, 102]
$R_{41} : e + Cl \rightarrow Cl(6s) + e$	12.1	$k_{58} = 1.27 \times 10^{-9} \exp(-11.0/Te)$	[103, 102]
$R_{42} : e + Cl \rightarrow Cl(5d) + e$	12.4	$k_{59} = 7.00 \times 10^{-9} \exp(-13.0/Te)$	[103, 101, 58, 60, 102]
Radiative desexcitation			
Reaction	Threshold Energy (eV)	Reaction rate ($\text{cm}^3.\text{s}^{-1}$)	ref
$R_{43} : Cl(4s) \rightarrow Cl + h\nu$	0.0	$k_{39} = 2.03 \times 10^6$	[101, 70]
$R_{44} : Cl(4p) \rightarrow Cl + h\nu$	0.0	$k_{40} = 3.3 \times 10^7$	[101, 70]
$R_{45} : Cl(3d) \rightarrow Cl + h\nu$	0.0	$k_{41} = 1.83 \times 10^6$	[101, 70]
$R_{46} : Cl(A, C) \text{ ou } Cl_2(B) \rightarrow Cl_2 + h\nu$	0.0	$k_{43} \text{ et } k_{44} = 4.74 \times 10^8$	[101, 70]

Table 10. Surface reactions for Cl_2 .

Reaction	β_{Cl}	Reaction rate ($\text{cm}^3.\text{s}^{-1}$)	ref
Neutrals-walls reactions, considering coefficient β at wall temperature			
$Rs_1 : Cl + wall \rightarrow 1/2 Cl_2 + wall$	0.13	$k_{s230} = \frac{D_{ab}}{\Lambda_0^2 + \frac{2l_0 D_{ab}}{v_{th}} + \frac{(2-\beta_{Cl})}{\beta_{Cl}}}$	[101]
$Rs_2 : Cl + wall \rightarrow Cl(4s, 4p, 3d) + wall$	0.13	$k_{230} = \frac{D_{ab}}{\Lambda_0^2 + \frac{2l_0 D_{ab}}{v_{th}} + \frac{(2-\beta_{Cl})}{\beta_{Cl}}}$	[101]
$Rs_3 : Cl(4s, 4p, 3d) + wall \rightarrow Cl + wall$	0.13	$k_{235} = \frac{D_{ab}}{\Lambda_0^2 + \frac{2l_0 D_{ab}}{v_{th}} + \frac{(2-\beta_{Cl})}{\beta_{Cl}}}$	[101]
$Rs_4 : Cl_2(A, C) \text{ ou } Cl_2(B) + wall \rightarrow Cl_2 + wall$	0.13	$k_{236} = \frac{D_{ab}}{\Lambda_0^2 + \frac{2l_0 D_{ab}}{v_{th}} + \frac{(2-\beta_{Cl})}{\beta_{Cl}}}$	[101]
Ions-walls reactions			
$Rs_5 : Cl^+ + wall \rightarrow Cl + wall^*$		$k_{18} = 2\mu_{B, Cl^+} \left(\frac{h_L}{L} + \frac{h_R}{R} \right)$	[55, 101]
$Rs_6 : Cl_2^+ + wall \rightarrow Cl_2 + wall^*$		$k_{11} = 2\mu_{B, Cl_2^+} \left(\frac{h_L}{L} + \frac{h_R}{R} \right)$	[55, 101]

Table 11. Species taken into account for pure Ar plasma.

Neutrals		Positive Ions	Excited states
Ar	Ar ⁺	Ar(<i>m</i>), Ar(<i>r</i>), Ar(4 <i>p</i>)	

Table 12. Reaction scheme for Ar plasma

Reaction	Threshold Energy (eV)	Reaction rate (cm ³ .s ⁻¹)	ref
Excitation and desexcitation by electronic impact (cm ³ .s ⁻¹)			
R ₁₀₀ : e + Ar → Ar(<i>m</i>) + e	11.7	k ₁₁₇ = 9.73 × 10 ⁻¹⁰ Te ^{-0.07} exp(-11.69/Te)	[55, 101, 58]
R ₁₀₁ : e + Ar → Ar(<i>r</i>) + e	11.8	k ₁₁₆ = 3.93 × 10 ⁻⁹ Te ^{0.46} exp(-12.09/Te)	[55, 101, 58]
R ₁₀₂ : e + Ar → Ar(4 <i>p</i>) + e	13.3	k ₁₀₁ = 8.91 × 10 ⁻⁹ Te ^{-0.04} exp(-14.18/Te)	[55, 101, 58]
R ₁₀₃ : e + Ar(<i>m</i>) → Ar(<i>r</i>) + e	0.1	k ₁₀₉ = 3.7 × 10 ⁻⁷	[55, 101, 58]
R ₁₀₄ : e + Ar(<i>m</i>) → Ar(4 <i>p</i>) + e	1.6	k ₁₁₅ = 2.39 × 10 ⁻⁶ Te ^{-0.15} exp(-1.82/Te)	[55, 101, 58]
R ₁₀₅ : e + Ar(<i>r</i>) → Ar(<i>m</i>) + e	-0.1	k ₁₀₆ = 9.1 × 10 ⁻⁷	[55, 101, 58]
R ₁₀₆ : e + Ar(<i>m</i>) → Ar + e	-11.7	k ₁₀₃ = 2.0 × 10 ⁻⁹	[55, 101, 58]
R ₁₀₇ : e + Ar(<i>r</i>) → Ar + e	-11.8	k ₁₀₃ = 2.0 × 10 ⁻⁹	[55, 101, 58]
R ₁₀₈ : e + Ar(4 <i>p</i>) → Ar + e	-13.3	k ₁₀₃ = 2.0 × 10 ⁻⁹	[55, 101, 58]
R ₁₀₈ : e + Ar → Ar + e	0.0	k ₁₀₇ = 2.16 × 10 ⁻⁷ exp($\frac{0.0607}{Te} - \frac{12.30}{Te^2} + \frac{14.20}{Te^3} - \frac{4.26}{Te^4}$)	[55, 101, 58]
Ionization by electronic impact (cm ³ .s ⁻¹)			
R ₁₀₉ : e + Ar → Ar ⁺ 2e	15.8	k ₁₀₀ = 2.39 × 10 ⁻⁸ Te ^{0.57} exp(-17.43/Te)	[55, 101, 58]
R ₁₁₀ : e + Ar(<i>m</i>) → Ar ⁺ 2e	4.1	k ₁₂₃ = 2.71 × 10 ⁻⁷ Te ^{0.26} exp(-4.59/Te)	[55, 101, 58]
R ₁₁₁ : e + Ar(<i>r</i>) → Ar ⁺ 2e	4.0	k ₁₂₄ = 2.7 × 10 ⁻⁷ Te ^{0.29} exp(-4.24/Te)	[55, 101, 58]
R ₁₁₂ : e + Ar(4 <i>p</i>) → Ar ⁺ 2e	2.5	k ₁₀₂ = 1.09 × 10 ⁻⁶ Te ^{0.29} exp(-3.42/Te)	[55, 101, 58]
Reactions between atoms and molecules (cm ³ .s ⁻¹)			
R ₁₁₃ : 2Ar(<i>m</i>) → 2Ar	0.0	k ₁₁₈ = 2.0 × 10 ⁻⁷	[55, 101, 58]
R ₁₁₄ : Ar(<i>m</i>) + Ar → 2Ar	0.0	k ₁₂₂ = 2.1 × 10 ⁻¹⁵	[55, 101, 58]
R ₁₁₅ : Ar(<i>m</i>) + Ar(<i>r</i>) → Ar ⁺ + Ar	0.0	k ₁₁₉ = 2.1 × 10 ⁻⁹	[55, 101, 58]
R ₁₁₆ : 2Ar(4 <i>p</i>) → Ar ⁺ + Ar	0.0	k ₁₂₀ = 5.0 × 10 ⁻¹⁰	[55, 101, 58]
R ₁₁₇ : 2Ar(<i>m</i>) → Ar ⁺ + Ar	0.0	k ₁₂₁ = 6.4 × 10 ⁻¹⁰	[55, 101, 58]
Radiative deexcitations (s ⁻¹)			
R ₁₁₈ : Ar(<i>r</i>) → Ar + hν	0.0	k ₁₂₅ = 1.0 × 10 ⁵	[55, 101, 58]
R ₁₁₉ : Ar(4 <i>p</i>) → Ar + hν	0.0	k ₁₂₆ = 3.2 × 10 ⁷	[55, 101, 58]
R ₁₂₀ : Ar(4 <i>p</i>) → Ar(<i>m</i>) + hν	0.0	k ₁₂₇ = 3.0 × 10 ⁷	[55, 101, 58]
Surface reactions (s ⁻¹)			
Rs ₁₀ : Ar ⁺ + wall → Ar + wall*	0.0	k _{s105} = 2μ _{B,Cl₂⁺} ($\frac{hL}{L} + \frac{hR}{R}$)	[55, 101, 58]